RESEARCH ARTICLE

WILEY

A time averaged steady state method for the Navier–Stokes equations

Mengjie Zhao[1] | **Rubén Zorrilla[2]** | **Riccardo Rossi[2,3]** | **Roland Wüchner[1,2]**

[1]Chair of Structural Analysis, Department of Civil, Geo and Environmental Engineering, Technical University of Munich, Munich, Germany

[2]Kratos Multiphysics group, International Centre for Numerical Methods in Engineering, Barcelona, Spain

[3]Department of Civil and Environmental Engineering (DECA), Polytechnic University of Catalonia (UPC), Barcelona, Spain

Correspondence
Mengjie Zhao, Department of Civil, Geo and Environmental Engineering, Technical University of Munich, Germany.
Email: mengjie.zhao@tum.de

Abstract

This work derives an incompressible variational multiscales time-averaged Navier–Stokes (NS) formulation that aims at obtaining accurate steady state solutions. Rather than using the standard time instantaneous velocity and pressure, the new formulation devises a time averaging procedure based on rewriting and solving the NS equations in terms of the newly defined time-averaged velocity and pressure. Hence, the method could be understood as a convenient change of variable so that the problem is rewritten directly in terms of the steady state quantities. The important advantage of such a point of view is that it can in principle be applied to any other formulation. Such time averaging procedure is complemented by two time step modification strategies in order to accelerate the convergence to the steady state. The guidelines of an integrated framework are presented in the article, starting with the description of the proposed numerical technique applied to general incompressible flows. The explanation is enhanced with a one-dimensional (1D) nonlinear oscillator example. Several results are presented concerning analytical benchmarks, simulation of flows in laminar, transitional and turbulent regimes with and without an inherently steady solution.

KEYWORDS

computational fluid dynamics, finite element method, Navier–Stokes, steady state, time-averaged, variational multiscale method

1 | INTRODUCTION AND MOTIVATION

1.1 | Background

Though computational fluid dynamics (CFD) is a relatively young principle. It is used today in the design phase of a wide variety of technical applications ranging from the automotive or aircraft industries to wind power generation. It is well known among all CFD disciplines that the simulation of turbulent fluid flows is always a problem because it is difficult to accurately predict the main characteristic features of such chaotic flows. When turbulence is present, it appears to dominate all other flow phenomena and improve mass, momentum transfer and energy dissipation. Because

of this complex and chaotic nature of turbulence flows, there are hardly any analytical solutions and the turbulences must therefore be modeled.

The turbulence can be categorized into three scales: the large scale, which accounts for the most momentum and energy transfer; the small scale, in which the energy dissipates; and the immediate scale which acts as energy transfer between the two scales.

In order to fully resolve the entire turbulent lengths and time scales, an extremely fine grid and small time steps are required to achieve a complete spatial and temporal resolution. This approach is known as direct numerical simulation (DNS) and requires an enormous and often prohibitive computational effort. As a result, even today this is only possible for flows with low Reynolds numbers.

Considering that goal of turbulence modeling in practice is to get a proper representation of the main flow features at a low computational cost, rather than a full representation of the turbulence, DNS is rarely used. Such a representation can either be one of the mean values or extremes. In the former case, the flow can be solved by directly calculating the statistical average of the solution. This is known as the Reynolds-averaged Navier–Stokes (RANS) approach, in which the flow quantities are decomposed into a statistical average and a fluctuation part in time. On the other hand, if instantaneous quantities are desired, a spatial filter is used instead of the temporal filter, which means that the flow quantities are decomposed into a resolved filtered part and a modeled subgrid-filtered part, leading to the known subgrid-scale modeling (SGS) approach.

One of the best-known techniques in the SGS family is the large Eddy simulation (LES) method, which is viewed as a compromise between accuracy and computational cost. Only large flow features, which are dependent on geometry and boundary conditions, are resolved directly, so that the small flow motions, which can be solved universally, independently of the problem and usually in a computationally intensive manner, can be modeled by an SGS model. LES techniques are gaining increasing attention in the CFD community due to their high accuracy and reliability in predicting turbulence.

Currently, the most widely used formulation in the industry is the finite volume RANS solver with second-order accuracy. Still, there are a large number of industrial CFD applications where flows with massive separation occur, while RANS models have had limited success in predicting steady flow. LES techniques are therefore addressed to predict such complex turbulent flow patterns.[1]

1.2 | Motivation

Time averaging solution represents a very interesting alternative for the case of bluff bodies. The time averaged equations can also be very interesting in connection with optimization, for example with minimizing wind load of high-rise structures or the optimizing the shale of automotive or aircraft structures. Roughly speaking, the main problem in such studies can be reduced to decrease the fluid forces exerted on the structure. This usually implies solving many trial models and configurations toward the most efficient and sustainable design. To speed up such design processes, faster steady solvers are likely to be employed, since in most cases only the net effects of turbulent fluctuations are relevant. As mentioned above, RANS is one of the most widely used solutions in industrial applications, because the average of the fluctuating part of the flow quantities is zero and the average of the temporally averaged part is kept the same, which means that the stationary solution can be obtained with less effort.

Whenever unsteady effects occur in flow analysis, steady solvers will have difficulties getting a converged result. In no particular order, such unsteady effects can be classified as follows. First, the waves formed on free surfaces can exhibit oscillatory effects that lead to unsteady motion. A second important topic is the large pressure surges that are generated by flows that are rapidly brought to rest. The third class of unsteady flows is inherently unstable, although steady boundary conditions are applied. A classic example of the latter is the flow of liquid past a circular cylinder.[2]

In these cases, unsteady formulations, such as unsteady Reynolds-averaged Navier–Stokes (URANS) and LES are usually applied to obtain time instantaneous flow quantities. Then, time averaged results can be obtained as postprocessing of such a time instantaneous solution. However, this procedure is much more time consuming as it typically requires more human and computational resources than the steady formulation alternatives. In addition, as the number of simulations required increases due to a large number of design parameters to be tested, its use becomes impossible. Last but not least, special care must be taken when selecting the turbulence models for the URANS solution. Otherwise, the result obtained can differ considerably from the actual flow behavior.

In this context, a fast, robust, universal steady solver capable of deriving a time averaged steady solution as well as if it had been averaged from the time instantaneous data is of interest for its practical application in solving practical technical problems. From a theoretical point of view, it is also interesting to investigate the existence and the accuracy of this time averaged steady solution.

1.3 | Objectives

This article aims to derive a new steady state formulation based on rewriting the Navier–Stokes (NS) equations with the time averaged flow quantities. In a sense, this can be thought of as a kind of RANS model where the closing equations are based solely on numerical correlations. The concept of this averaging technique is based on the observation that there is always a *a posteriori* steady solution (provided that the flow field is averaged over a sufficient time span). Solving the NS equations, in which the instantaneous quantities are replaced by time averaged ones, will therefore leads to a steady solution. Although the time accurate and time averaged formulations describe the same physics, the latter has the advantage of having a better conditioned matrix system so that it is inherently easier to solve. Another advantage of this averaging technique over the time-instantaneous solver is that the time step can be increased to accelerate the convergence to the steady state since only the steady state solution is desired, while for the transient solver, increasing the time step may cause instability problems.

The following describes how the article is organized. First the formulation and the time averaging technique are presented. After that, the proposed technique will be applied to an academic example (1D nonlinear oscillator) to test its capabilities and facilitate discussion. In the following sections, the accuracy and robustness of the time averaging technique presented will be examined using reference flow problems with and without a steady solution. In addition, some acceleration methods based on the time step size increment are analyzed and compared with the reference solutions. The last chapter summarizes the most important results and achievements of the work.

All the formulations presented in this work have been implemented within the open source finite element (FE) framework KratosMultiphysics (a.k.a. Kratos).[3,4] Kratos is completely object-oriented and written in C++ with a Python interface. It also offers shared (OpenMP) and distributed (MPI) parallelization capabilities. Matplotlib, GiD and ParaView have been used for the postprocessing of the results.

2 | FORMULATION

Fluid flows are mainly characterized by the fluid properties (viscosity, compressibility), by the object geometry, which influences the spatial variations, and by the time variations or unsteadiness. All these factors are taken into account simultaneously by the NS equations. However, only a few flow problems can be solved analytically using such a mathematical model, and these are either laminar flows or flows around simple geometries, which implies introducing multiple simplifying assumptions. For more complex flow problems, which attempt to represent viscous effects and resolve turbulence, the NS equations need to be solved using approximating techniques (numerical methods).

In the following, the viscous incompressible NS equations will be derived and its discretization using the finite element method (FEM) together with the variational multiscale stabilization method (VMS) is presented.

2.1 | The NS equations

The NS equations are derived from the laws of mass and momentum conservations. The former implies that mass within a fluid system is preserved and never created nor destroyed if there are no mass sources or sinks. The latter states the force equilibrium, which is to say that the rate of change in momentum of a fluid system is equal to the net forces acting on it.

With $\mathbf{u}$ denoting the velocity, p the pressure, $\boldsymbol{\sigma}$ the Cauchy stress tensor, ρ the fluid density, $\mathbf{f}$ the body forces and $\partial(\cdot)/\partial t$ the partial time derivative, the incompressible NS equations in the fluid domain Ω are given as:

$$\rho \frac{\partial \mathbf{u}}{\partial t} - \boldsymbol{\nabla} \cdot \boldsymbol{\sigma} + \rho \mathbf{u} \cdot \boldsymbol{\nabla} \mathbf{u} = \mathbf{f} \text{ in } \Omega, \tag{1a}$$

$$\nabla \cdot \mathbf{u} = 0 \text{ in } \Omega. \tag{1b}$$

The problem above is only well defined when proper initial and boundary conditions are provided. These are:

$$\mathbf{u} = \mathbf{u_0} \text{ in } \Omega, \ t = 0, \tag{2a}$$

$$\mathbf{u} = \bar{\mathbf{u}} \text{ on } \Gamma_D \times [0, T], \tag{2b}$$

$$\mathbf{t} = \bar{\mathbf{t}} \text{ in } \Gamma_N \times [0, T]. \tag{2c}$$

where $\mathbf{u_0}$ is the initial velocity field, Γ_D denotes the Dirichlet boundary and Γ_N denotes the Neumann boundary. $\bar{\mathbf{u}}$ is the velocity imposed on Γ_D and $\mathbf{t}$ is the Cauchy traction vector, the definition of which is $\mathbf{t} = \boldsymbol{\sigma} \cdot \mathbf{n}$, with $\mathbf{n}$ being the surface outer normal vector and $\bar{\mathbf{t}}$ the imposed traction on the Neumann boundary Γ_N.

In this work, only isotropic incompressible fluids are considered. This allows to reduce the Cauchy stress tensor to:

$$\boldsymbol{\sigma} = -p\mathbf{I} + \boldsymbol{\tau}, \tag{3}$$

where $\mathbf{I}$ is the second-order identity tensor and $\boldsymbol{\tau}$ is the viscous shear stress tensor. For a Newtonian fluid, the viscous shear stress is defined as

$$\boldsymbol{\tau} = 2\mu \left(\boldsymbol{\nabla}^s \mathbf{u} - \frac{1}{3}(\nabla \cdot \mathbf{u}) \right) \tag{4}$$

with μ being the dynamic viscosity of the fluid and $\boldsymbol{\nabla}^s \mathbf{u}$ the symmetric gradient of velocity, which is computed as

$$\boldsymbol{\nabla}^s \mathbf{u} = \frac{1}{2} \left(\boldsymbol{\nabla}\mathbf{u} + (\boldsymbol{\nabla}\mathbf{u})^T \right). \tag{5}$$

By substituting the Cauchy stress tensor definition in Equation (3) into the NS equations in Equation (1a), the well-known NS equations for purely incompressible Newtonian fluids are obtained as:

$$\rho \frac{\partial \mathbf{u}}{\partial t} + \nabla p - \nabla \cdot 2\mu \left(\boldsymbol{\nabla}^s \mathbf{u} - \frac{1}{3}(\nabla \cdot \mathbf{u}) \right) + \rho \mathbf{u} \cdot \boldsymbol{\nabla}\mathbf{u} = \mathbf{f}, \tag{6a}$$

$$\boldsymbol{\nabla} \cdot \mathbf{u} = 0. \tag{6b}$$

2.2 | Weak form of NS equations

The Navier–Stokes equations can be approximated with different numerical techniques, among which the most extended one is the finite volume method (FVM). This discretization method, often used alongside with RANS models, has the advantage of preserving the conservation of mass and momentum inside each cell thanks to the nature of its formulation, so that no extra stabilization is needed. The FEM provides a much different formulation governed by the principle of minimum energy. For any boundary value problem, this principle guarantees that the obtained solution is the one that minimizes the total energy. A major difference between the FEM and the FVM approaches is that the FEM adopts the weak form of the governing equations instead of the integral form in the FVM.[5] Moreover, the FEM features a polynomial approximation of the integrated quantities. This is achieved by means of the so-called shape functions, which are continuous from one element to its neighbors. The FEM additionally needs to take the stability conditions into account, which adds further complexity to its formulation. In this work, the FEM method, in combination with the VMS stabilization technique, is employed. In the following, this stabilized FE formulation for the viscous incompressible NS equations is derived.

In the FE formulation of the NS equations, the mass and momentum are only preserved in a weak sense, which means that only the integral of the conversation equations over the problem domain is preserved. This is expressed by the so-called weak form of the problem, which is obtained by multiplying the integral form of the momentum conservation equations by a velocity test function $\mathbf{w}$, defined to be zero on the Dirichlet boundary Γ_D, and the mass conservation equation by a pressure test function q. Thus, the weak form of the NS equations reads as:

$$\int_\Omega \mathbf{w} \cdot \left(\rho \frac{\partial \mathbf{u}}{\partial t} - \nabla \cdot \boldsymbol{\sigma} + \rho \mathbf{u} \cdot \nabla \mathbf{u} \right) d\Omega = \int_\Omega \mathbf{w} \cdot \mathbf{f} \, d\Omega, \tag{7a}$$

$$\int_\Omega q \nabla \cdot \mathbf{u} \, d\Omega = 0. \tag{7b}$$

Equation (7a) is integrated by parts to make it possible to apply Neumann boundary conditions. After this operation to the weak form of the momentum conservation equation, the final weak form of the NS equations is obtained as:

$$\int_\Omega \mathbf{w} \cdot \left(\rho \frac{\partial \mathbf{u}}{\partial t} + \rho \mathbf{u} \cdot \nabla \mathbf{u} \right) d\Omega + \int_\Omega \nabla^s \mathbf{w} : 2\mu \left(\boldsymbol{\nabla}^s \mathbf{u} - \frac{1}{3} (\nabla \cdot \mathbf{u}) \right) d\Omega - \int_\Omega p \boldsymbol{\nabla} \cdot \mathbf{w} \, d\Omega = \int_\Omega \mathbf{w} \cdot \mathbf{f} \, d\Omega + \int_{\Gamma_N} \mathbf{w} \cdot \mathbf{t} \, d\Gamma, \tag{8a}$$

$$\int_\Omega q \boldsymbol{\nabla} \cdot \mathbf{u} \, d\Omega = 0. \tag{8b}$$

As mentioned above, the complex nature of turbulent flows (three-dimensional [3D], high unsteadiness, and complex flow patterns at a multitude of different sizes) requires a prohibitive amount of elements and time steps to properly represent the full range of turbulent motions, even at a moderately low Reynolds number. To avoid the use of such a DNS approach, it is required to model the small unresolved scales, since only large scales can be afforded to be resolved. One of the most common turbulence modeling techniques is the LES, which separates the small scales from the large scales through a spatial convolutional filter. The assumptions taken to perform such convolution is known to imply nonnegligible errors in bounded domains.[6,7]

In this context, a promising idea to avoid these problems is to separate turbulent scales into appropriate spaces using variational projections, which leads to the aforementioned VMS methods.

2.3 | VMS methods

The VMS method was first proposed by Hughes.[8] The main idea of the method is to decompose the FE space into the sum of coarse (large) and fine (small) scale components, which are related by a projection operation. In the following, the derivation of the variational form of the viscous incompressible NS together with a VMS stabilization technique is presented.

Denoting the large-scale magnitudes with a subscript $(\cdot)_h$ and the small scale (or subscale) ones with a subscript $(\cdot)_s$, the flow quantities be decomposed into

$$\mathbf{u} = \mathbf{u}_h + \mathbf{u}_s, \tag{9a}$$

$$p = p_h + p_s. \tag{9b}$$

The same decomposition can also be applied to the test functions as

$$\mathbf{w} = \mathbf{w_h} + \mathbf{w_s}, \tag{10a}$$

$$q = q_h + q_s. \tag{10b}$$

The large-scale solutions $\mathbf{u}_h \in W_h \subset W$ and $p_h \in Q_h \subset Q$ are defined in the finite-dimensional space W_h and Q_h and the subscale solutions $\mathbf{u}_s \in W_s \subset W$ and $p_s \in Q_s \subset Q$ the complement of the small scale solution in the infinite L^2 space. It holds:

$$W = W_h \oplus Ws, \quad Q = W_h \oplus Q_s. \tag{11}$$

Rewriting the NS equations in the residual form:

$$\mathbf{R}^m(\mathbf{u}, p) = \mathbf{f} - \rho \frac{\partial \mathbf{u}}{\partial t} - \rho \mathbf{u} \cdot \nabla \mathbf{u} - \nabla p + 2\mu \nabla \cdot (\nabla^s \mathbf{u} - \frac{1}{3}(\nabla \cdot \mathbf{u})\mathbf{I}), \tag{12a}$$

$$R^c(\mathbf{u}) = -\nabla \cdot \mathbf{u} \tag{12b}$$

with $\mathbf{R}^m(\mathbf{u}, p)$ denoting the residual of the momentum conservation equation and $R^c(\mathbf{u}, p)$ denoting the residual of the continuity equation, the weak form of the set of NS equations can be rewritten as follows:

$$\left(\mathbf{w}, \mathbf{R}^m(\mathbf{u}, p)\right)_\Omega = 0, \tag{13a}$$

$$\left(q, R^c(\mathbf{u})\right)_\Omega = 0. \tag{13b}$$

Extra equations are required to solve the unknown subscale variables. These subscale equations can then be written in terms of the residual form of the NS equations applied to the large-scale variables $\mathbf{R}^m(\mathbf{u}_h, p_h)$ and $R^c(\mathbf{u}_h)$:

$$\rho \mathbf{u} \cdot \nabla \mathbf{u}_s + \nabla p_s - 2\mu \nabla \cdot \left(\nabla^s \mathbf{u}_s - \frac{1}{3}(\nabla \cdot \mathbf{u}_s)\mathbf{I}\right) = \mathbf{R}^m(\mathbf{u}_h, p_h) - \boldsymbol{\xi}_h, \tag{14a}$$

$$\nabla \cdot \mathbf{u}_s = R^c(\mathbf{u}_h) - \delta_h \tag{14b}$$

with $\boldsymbol{\xi}_h$ and δ_h depending on the projection from the continuous L^2 to the subscale space, chosen in such a way that the right-hand sides of Equations (14a) and (14b) belong to the corresponding small scale space W_s and Q_s. Since the small scale spaces are as well infinite as the continuous space, Equations (14a) and (14b) need to be approximated before they can be solved. In practice, the definition of an approximate small scale space corresponds to a choice of projectors from the L^2 to the subscale space. The simplest and most straightforward projection is to the identity projection, which is equivalently to $\boldsymbol{\xi}_h = 0$ and $\delta_h = 0$. This approach is known as the algebraic subgrid scale (ASGS) method.

Since the calculation of $\boldsymbol{\xi}_h$ and δ_h is coupled with the FE solutions $\mathbf{u}_h$ and p_h, it will either double the number of nodal degrees of freedom of the problem, or require additional implementation to solve it in a staggered way. In practice, since that the NS equations are nonlinear and have to be solved iteratively anyway, the projection problem can be implemented in a staggered way, updating the projections after each nonlinear NS iteration. Therefore, the problem for the small scales, given by Equation (14), is usually not solved. Instead, they are usually approximated by an expression of the form:

$$\rho \frac{\partial \mathbf{u}_s}{\partial t} + \frac{1}{\tau_u} \mathbf{u}_s \approx \mathbf{R}^m(\mathbf{u}_h, p_h) - \boldsymbol{\xi}_h, \tag{15a}$$

$$\frac{1}{\tau_p} p_s \approx R^c(\mathbf{u}_h) - \delta_h, \tag{15b}$$

where second-order tensor $\boldsymbol{\tau}_u$ and the scalar τ_p, known as stabilization parameters, are algorithmic quantities that need to be modeled. A motivation for Equation (15) can be found in Reference 9, where the parameters in Equation (15) are designed to ensure that the L_2 norm of the modeled subscale variables and the exact small scale values are equivalent. While Equation (15) represents the complete small scale model derived from the dynamic NS equations, there are many VMS formulations in the literature, where the time variation of the velocity small scale model is be neglected. This approach is called quasi-static small scale model, which is advantageous to employ when a steady state solution is desired. With the quasi-static small scale model that the small scales can be defined as:

$$\mathbf{u}_s \approx \tau_u \mathbf{R}^m(\mathbf{u}_h, p_h - \boldsymbol{\xi}_h), \tag{16a}$$

$$p_s \approx \tau_p R^c(\mathbf{u}_h - \delta_h). \tag{16b}$$

The equations above assume that the velocity small scales $\mathbf{u}_s$ adapt automatically to the large-scale residuals $\mathbf{R}^m$ and R^c. In order to complete the formulation, a definition for the stabilization parameters is required. Following the approach described in Reference 10, the velocity stabilization parameter $\boldsymbol{\tau}_u$ is taken to be a diagonal matrix $\boldsymbol{\tau}_u = \tau_u \mathbf{I}$ while τ_u and τ_p are defined as

$$\tau_u = \left(\frac{c_1 \mu}{h^2} + \frac{c_2 \rho \|\mathbf{u}_h\|}{h}\right)^{-1}, \tag{17a}$$

$$\tau_p = \frac{h^2}{c_1 \tau_u}, \tag{17b}$$

where c_1 and c_2 are constant, which are commonly defined as $c_1 = 4$, $c_2 = 2$ for linear elements and h is the characteristic element size. With the small scale model defined, the final Galerkin residual weak form can be derived, which is written as follows:

$$\int_\Omega \mathbf{w}_h \rho \left(\frac{\partial \mathbf{u}_h}{\partial t} + \mathbf{u}_h \nabla \cdot \mathbf{u}_h \right) \, d\Omega$$

$$+ \int_\Omega \nabla^s \mathbf{w}_h : 2\mu \left(\nabla^s \mathbf{u}_h - \frac{1}{3} (\nabla \cdot \mathbf{u}_h) \mathbf{I} \right) \, d\Omega - \int_\Omega (\nabla \cdot \mathbf{w}_h) p_h \, d\Omega$$

$$- \int_\Omega \rho (\mathbf{u}_h \cdot \nabla \mathbf{w}_h) \tau_u \mathbf{R}^m (\mathbf{u}_h, \mathbf{p}_h) \, d\Omega$$

$$- \int_\Omega \nabla \cdot \mathbf{w}_h \tau_p R^c (\mathbf{u}_h) \, d\Omega$$

$$= \int_\Omega \mathbf{w}_h \mathbf{f} \, d\Omega + \int_{\Gamma_N} \mathbf{w}_h \mathbf{t} \, d\Gamma, \tag{18a}$$

$$\int_\Omega q_h \nabla \cdot \mathbf{u}_h \, d\Omega - \int_\Omega \nabla q_h \tau_u \mathbf{R}^m (\mathbf{u}_h, p_h) \, d\Omega = 0, \tag{18b}$$

where $\mathbf{t} = (2\mu : \nabla^s \mathbf{u}_h - p_h \mathbf{I}) \cdot \mathbf{n}$ is the Cauchy traction vector with $\mathbf{n}$ the boundary outwards unit vector. Γ_N is the Neumann boundary. The first two rows in Equation (18a) in combination with its right-hand side, constitute the standard Galerkin discretization of the momentum equation. The third row in Equation (18a) model the velocity small scale on the large-scale equations, while the last row of Equation (18a) represents the effect of pressure small scales. Analogously, the first term of Equation (18b) represents the Galerkin weak form of the incompressibility equation, while the second term models the effect of the small scales in mass conservation.

2.4 | Discretization

Before the VMS equation in Equation (18) can be solved numerically, it first need to be discretize in space and time. Introducing a FE partition Ω_h for domain Ω, the large scale part of the solution, $\mathbf{u}_h$ and p_h can be approximated by standard FE basis functions as

$$\mathbf{u}_h = \sum_{i=1}^{n_n} \mathbf{N}_i(x) \mathbf{u}_i, \tag{19a}$$

$$p_h = \sum_{i=1}^{n_n} N_i(x) p_i, \tag{19b}$$

where n_n represents the number of nodes in the FE mesh, $\mathbf{u_i}$ and p_i are the nodal values of the large-scale variables $\mathbf{u}_h$ and p_h, respectively, N_i represents the standard FE basis function associated to node i and $\mathbf{N_i}$ its vectorial counterpart. For a quasi-static ASGS formulation, the algebraic discrete form of Equation (18) is

$$[\mathbf{M} + \mathbf{S}_m(\tau_u, \mathbf{u}_h)] \dot{\mathbf{U}} + [\mathbf{C}(\mathbf{u}_h) + \mathbf{K} + \mathbf{S}_u(\tau_u, \mathbf{u}_h) + \mathbf{H}_u(\tau_u))] \mathbf{U} + [\mathbf{G} + \mathbf{S}_p(\tau_u, \mathbf{u}_h)] \mathbf{P} = \mathbf{F} + \mathbf{T} + \mathbf{S}_f(\tau_u, \mathbf{u}_h), \tag{20a}$$

$$\mathbf{Q}_m(\tau_u) \dot{\mathbf{U}} + [\mathbf{D} + \mathbf{Q}_u(\tau_u, \mathbf{u})] \mathbf{U} + \mathbf{Q}_p(\tau_u) \mathbf{P} = \mathbf{Q}_f(\tau_u), \tag{20b}$$

where $\mathbf{U}$, $\dot{\mathbf{U}}$ and $\mathbf{P}$ are the vectors of nodal velocity, acceleration and pressure, respectively. Equation (20) is the discrete version of the Equation (18) and can be built from the assembly of elemental contributions. In general, a matrix $\mathbf{A}$ is constructed by the FE assembly of elemental matrices of the form $\mathbf{A}^e$. The standard Galerkin terms and the stabilization terms in Equation (20) are given in the Appendix A. For detailed derivations, please refer to Cotela.[11] Without loss of generality, Equation (20) can be rewritten into an equivalent matrix form:[11]

$$\tilde{\mathbf{M}} \begin{bmatrix} \dot{\mathbf{U}} \\ \mathbf{0} \end{bmatrix} + \tilde{\mathbf{C}} \begin{bmatrix} \mathbf{U} \\ \mathbf{P} \end{bmatrix} = \tilde{\mathbf{F}}. \tag{21}$$

The Equation (21) still requires to be discretized in time. Here a second-order backward differentiation formula (BDF2)[12] is applied owing to its reported stability and accuracy in similar problems.[13,14] For a constant time step Δt, the BDF2 approximation of the acceleration $\dot{\mathbf{U}}_{n+1}$ reads

$$\dot{\mathbf{U}}_{n+1} = \frac{1}{\Delta t}\left(\frac{3}{2}\mathbf{U}_{n+1} - 2\mathbf{U}_n + \frac{1}{2}\mathbf{U}_{n-1}\right). \tag{22}$$

In order to reduce the simulation time or to alleviate some stability issues it might be convenient to use an adaptive BDF2 formula with varying time step. In the context of this article, using an adaptive BDF2 formula will make possible to accelerate the simulation wall time required by time averaging procedure to reach convergence. Hence, the time step size ratio $r_{n+1} = \Delta t_{n+1}/\Delta t_n$, which is computed from the current and previous time steps $\Delta t_{n+1} = t_{n+1} - t_n$ and $\Delta t_n = t_n - t_{n-1}$ is introduced. This allows to write the adaptive time step BDF2 formula, which is described for instance in Reference 15, as

$$\dot{\mathbf{U}}_{n+1} = \left(\frac{1+2r_{n+1}}{\Delta t_{n+1}(1+r_{n+1})}\right)\mathbf{U}_{n+1} - \left(\frac{1+r_{n+1}}{\Delta t_{n+1}}\right)\mathbf{U}_n + \left(\frac{r_{n+1}^2}{\Delta t_{n+1}(1+r_{n+1})}\right)\mathbf{U}_{n-1}. \tag{23}$$

By further introducing the following notation for the adaptive BDF2 coefficients

$$\omega_0 = \frac{1+2r_{n+1}}{\Delta t_{n+1}(1+r_{n+1})}$$
$$\omega_1 = -\frac{1+r_{n+1}}{\Delta t_{n+1}}$$
$$\omega_2 = \frac{r_{n+1}^2}{\Delta t_{n+1}(1+r_{n+1})} \tag{24}$$

in which the $n+1$ subscript is omitted to reduce the clutter, the Equation (21) can be discretized in time as

$$\left(\omega_0\tilde{\mathbf{M}} + \tilde{\mathbf{C}}\right)\begin{bmatrix}\mathbf{U}_{n+1}\\\mathbf{P}_{n+1}\end{bmatrix} = \tilde{\mathbf{F}} - \omega_1\tilde{\mathbf{M}}\begin{bmatrix}\mathbf{U}_n\\\mathbf{0}\end{bmatrix} - \omega_2\tilde{\mathbf{M}}\begin{bmatrix}\mathbf{U}_{n-1}\\\mathbf{0}\end{bmatrix}. \tag{25}$$

3 | TIME AVERAGING TECHNIQUE

In RANS formulations, flow variables are decomposed into a temporally averaged component and an instantaneous fluctuation from the temporal mean. While the temporally averaged variables are solved, the instantaneous fluctuation needs to be modeled as a result of the closure problem. Unlike the RANS formulation, the flow variables are temporally averaged with the instantaneous fluctuations. If a transient problem is solved, temporally averaging the flow quantities in a posteriori will always deliver a result, in which a steady solution exists in the sense that the time averaged value of the flow quantities does not vary in time, given that the time in which the flow variables are averaged is sufficiently long. This observation brings up the question of whether the flow variables can be averaged in a priori and solved directly with these time averaged variables. And if the flow problem can be indeed solved with the time averaged variables, what are the advantages of solving with time averaged quantities. In the following, these questions will be answered.

3.1 | Time averaged NS VMS formulation

Assuming an instantaneous flow solution is available, the time averaged solution of such instantaneous solution can be defined as the sum of the solutions at each instantaneous time slice weighted by its time step over the entire time. Following this definition, the averaged velocity $\bar{\boldsymbol{u}}_{n+1}$ and pressure $\bar{p}_{n+1}$ at time step $n+1$ with a variable time step size Δt_{n+1} can be defined as follows

$$\bar{\boldsymbol{u}}_{n+1} = \frac{\sum_{i=1}^{n+1}\boldsymbol{u}_i\Delta t_i}{t_{n+1}}, \tag{26a}$$

$$\overline{p}_{n+1} = \frac{\sum_{i=1}^{n+1} p_i \Delta t_i}{t_{n+1}}, \tag{26b}$$

where the overbar ($\overline{\bullet}$) denotes the time averaged quantities, $\boldsymbol{u}_i$ and p_i are the time instantaneous velocity and pressure at time step i and Δt_i is the corresponding time step size.

To solve the flow equations with solely time averaged quantities, instantaneous flow quantities need to be replaced by time averaged quantities. Solving at time step $n+1$, the instantaneous quantities can be expressed as a linear combination of the time averaged quantities at time step $n+1$ and n as

$$\boldsymbol{u}_{n+1} = \alpha_{n+1}\overline{\boldsymbol{u}}_{n+1} + \beta_{n+1}\overline{\boldsymbol{u}}_n, \tag{27a}$$

$$p_{n+1} = \alpha_{n+1}\overline{p}_{n+1} + \beta_{n+1}\overline{p}_n \tag{27b}$$

with α_{n+1} and β_{n+1} being constant factors at time step $n+1$. The values of α_{n+1} and β_{n+1} can be easily obtained by decomposing one of the averaged quantities into a time averaged part and an time instantaneous one. By doing so for $\overline{\boldsymbol{u}}_{n+1}$ it is obtained that

$$\overline{\boldsymbol{u}}_{n+1} = \frac{\Delta t_{n+1}\boldsymbol{u}_{n+1} + \sum_{i=1}^{n} \boldsymbol{u}_i \Delta t_i}{t_{n+1}}.$$

By applying the average definition in Equation (26), the previous equation can be equivalently expressed as

$$\overline{\boldsymbol{u}}_{n+1} = \frac{\Delta t_{n+1}}{t_{n+1}}\boldsymbol{u}_{n+1} + \frac{t_n}{t_{n+1}}\overline{\boldsymbol{u}}_n \rightarrow \boldsymbol{u}_{n+1} = \frac{t_{n+1}}{\Delta t_{n+1}}\overline{\boldsymbol{u}}_{n+1} - \frac{t_n}{\Delta t_{n+1}}\overline{\boldsymbol{u}}_n. \tag{28}$$

Comparing Equation (28) with Equation (27) shows that the α_{n+1} and β_{n+1} factors can be computed for any time averaged variable as

$$\alpha_{n+1} = \frac{t_{n+1}}{\Delta t_{n+1}}, \tag{29a}$$

$$\beta_{n+1} = -\frac{t_n}{\Delta t_{n+1}}. \tag{29b}$$

Finally, instead of solving Equation (25) with the time instantaneous quantities, the system of equations is rearranged in order to directly solve with the time averaged magnitudes. After introducing the definitions in Equation (27b), the time averaged system of equations reads

$$\left(\omega_0 \tilde{\mathbf{M}} + \tilde{\mathbf{C}}\right) \begin{bmatrix} \overline{\mathbf{U}}_{n+1} & \overline{\mathbf{U}}_n \\ \overline{\mathbf{P}}_{n+1} & \overline{\mathbf{P}}_n \end{bmatrix} \begin{bmatrix} \alpha_{n+1} \\ \beta_{n+1} \end{bmatrix} = \tilde{\mathbf{F}} - \omega_1 \tilde{\mathbf{M}} \begin{bmatrix} \overline{\mathbf{U}}_n & \overline{\mathbf{U}}_{n-1} \\ 0 & 0 \end{bmatrix} \begin{bmatrix} \alpha_n \\ \beta_n \end{bmatrix} - \omega_2 \tilde{\mathbf{M}} \begin{bmatrix} \overline{\mathbf{U}}_{n-1} & \overline{\mathbf{U}}_{n-2} \\ 0 & 0 \end{bmatrix} \begin{bmatrix} \alpha_{n-1} \\ \beta_{n-1} \end{bmatrix}. \tag{30}$$

3.2 | Steady state measurement

Any fluid can be considered steady when all the characteristic quantities do not vary in time. In continuous time, this means that the time derivative of all the flow quantities remains zero. In discrete time, this can be understood as a constant zero difference in the flow quantifies between the current step and the previous one.

Taking into account that absolutely steady flow rarely occur, it is more appropriate to refer to quasi-steady flows, in which the overall changes taking place over a period of time is considerably small. This can even occur for turbulent flows, which feature a continuous variation in the characteristic flow quantities due to the irregular motions of the fluid particles. However, despite such instantaneous fluctuations, the mean value of the instantaneous quantities can reach a quasi-steady state, which can be interpreted as steady-in-mean or a time averaged steady state, when a sufficiently long time period is given.

Following the previous definition of a discrete in time steady flow, it can be said the time averaged steady in a discrete time is reached when

$$\left\| \frac{\int_\Omega (\bar{\boldsymbol{u}}_{n+1} - \bar{\boldsymbol{u}}_n) d\Omega}{\Delta t} \right\| < \varepsilon \tag{31a}$$

$$\left| \frac{\int_\Omega (\bar{p}_{n+1} - \bar{p}_n) d\Omega}{\Delta t} \right| < \varepsilon. \tag{31b}$$

with $\varepsilon \geq 0$ sufficiently small.

Taken the space discretization into account, an overall time averaged steady state in a computational domain is reached when the sum of the rate of change of the flow quantities inside all elements converges to zero. Here two monitoring quantities are introduced to measure the steadiness. The first one is the magnitude of the rate of change in time averaged velocity $|\dot{\bar{\boldsymbol{u}}}|$ while the second one is the absolute value of the rate of change in time averaged pressure $|\dot{\bar{p}}|$. $|\dot{\bar{\boldsymbol{u}}}|$ and $|\dot{\bar{p}}|$ can be mathematically expressed as

$$\left\| \dot{\bar{\boldsymbol{u}}} \right\| = \frac{1}{A} \sum_{i=1}^{n_n} \left\| \frac{\bar{\boldsymbol{u}}_{n+1}^i - \bar{\boldsymbol{u}}_n^i}{\Delta t_n} \right\| A_i. \tag{32a}$$

$$|\dot{\bar{p}}| = \frac{1}{A} \sum_{i=1}^{n_n} \left| \frac{\bar{p}_{n+1}^i - \bar{p}_n^i}{\Delta t_n} \right| A_i, \tag{33a}$$

where A_i is the nodal area (volume) at node i and A is the area (volume) of the entire computational domain.

3.3 | Time averaging acceleration

For solutions of NS equations with different time scales, that is, solutions that change rapidly in some regions of the time domain while slowly changing in other regions, it is often beneficial to employ variable step sizes in order to obtain accurate and computationally efficient results. For example, small time steps may be required to capture rapidly changing initial solutions, while large time steps may be desirable to capture the subsequent, slowly changing, long-term evolution of the system.[16] Since the change time averaged quantities is slowing down as time evolves, the time step size can be enlarged to accelerate the convergence towards the steady state.

In this article, two acceleration formulations were investigated. Both time step acceleration strategies start with a time step size satisfying an initial Courant–Friedrichs–Lewy (CFL) number equal to 1. It is assumed that the CFL number of the problem equals the maximum element-wise CFL number, which is computed from each component of the element velocity projected along the corresponding element size. For a computational mesh Ω_e, this can be mathematically expressed as

$$\text{CFL} = \Delta t \max_{e \in \Omega_e} \left(\sum_{d=1}^{n_d} \frac{u_{x_d}^e}{h_d^e} \right), \tag{34}$$

where n_d is the problem dimension (2 in 2D and 3 in 3D), $u_{x_d}^e$ is the d-component of element velocity (i.e., midpoint velocity) and h_d^e is the element size in the x_d direction.

The previous definition of the CFL number allows to propose the next two following strategies to calculate the varying time step size Δt_{n+1}:

3.3.1 | Exponential growth

The first strategy for the time step acceleration is to use a geometric progression. Hence, the current time step size Δt_{n+1} is obtained from the previous one Δt_n and the user-defined time step ratio r as

$$\Delta t_{n+1} = \Delta t_n r. \tag{35}$$

Given the initial time step size Δt_0, the current time t_{n+1} can be also computed as

$$t_{n+1} = \sum_{i=0}^{n} \Delta t_{i+1} = \Delta t_0 \sum_{i=0}^{n} r^{i+1}. \tag{36}$$

3.3.2 | Linear interpolation

The second time step acceleration strategy is based on a linear interpolation of the CFL number. Thus, the sought CFL number at the current time step $\overline{\text{CFL}}_{n+1}$ is defined from the linear interpolation of the user-defined maximum and minimum CFL numbers CFL_{max} and CFL_{min} as

$$\overline{\text{CFL}}_{n+1} = \text{CFL}_{\text{min}} + \frac{t_n}{t_{\text{end}}}(\text{CFL}_{\text{max}} - \text{CFL}_{\text{min}}) \tag{37}$$

with t_{end} being the simulation end time. Then $\overline{\text{CFL}}_{n+1}$ is employed to obtain the current time step size Δt_{n+1}. Derived from Equation (34), it holds

$$\Delta t_{n+1} = \frac{\overline{\text{CFL}}_{n+1}}{\max\limits_{e \in \Omega_e} \left(\sum_{d=1}^{n_d} \frac{u_{x_d}^e}{h_d^e} \right)} \tag{38}$$

from which the next simulation time can be obtained as $t_{n+1} = t_n + \Delta t_{n+1}$. The effect of the time step size acceleration is analyzed based on the backward facing step (BFS) case, the results of which are discussed in Section 5.

3.4 | Time step stabilization

While it is computationally expensive to obtain results with a small time step size, a large step size can lead to nonphysical oscillations, which may eventually compromise the convergence of the numerical simulation. In consequence, it is commonly difficult to balance fast convergence and stability. This becomes even worse when the time discretization scheme is not unconditionally stable and time step size is limited by a stability condition.

Even though the time averaged formulation tolerates better large time steps, allowing thus to accelerate the time step by degrees, it can still suffer from stability problems coming from an aggressive time step size acceleration strategy. In Reference 17 Jannelli and Fazio suggest the use of a monitoring function to automate the selection of the time step size in problems involving stiff ODEs. In Reference 18 this approach is generalized to nonlinear PDEs.

Based on these ideas, the approach in Equation (39) is proceeded. If the monitor function η_n indicates that a time step is too large, that is, $\eta_n > \eta_{\text{max}}$, the time step size at next time step will be reduced. On the contrary, if $\eta_n < \eta_{\text{min}}$, the step size will be increased for the next time step with a chosen acceleration strategy. If these conditions do not hold, meaning that $\eta_{\text{min}} \leq \eta_n \leq \eta_{\text{max}}$, the time step size remains constant

$$\Delta t_{n+1} = \begin{cases} f(\Delta t_n) & \eta_n < \eta_{\text{min}}, \\ \Delta t_n & \eta_{\text{min}} \leq \eta_n \leq \eta_{\text{max}}, \\ g(\Delta t_n) & \eta_n > \eta_{\text{max}} \end{cases} \tag{39}$$

where $f(\Delta t_n)$ is a monotonically increasing function with respect to Δt_n while $g(\Delta t_n)$ is a monotonically decreasing function. In the case of exponentially growing time step size, $f = r\Delta t_n$ and $g = r^{-1}\Delta t_n$ with $r > 1$. In the case of linearly growing CFL number, $f = \Delta t_n + \Delta t_c$ and $f = \Delta t_n - \Delta t_c$ with $\Delta t_c > 0$. For the monitor function, Jannelli and Fazio[17] and Denner[18] chose the relative change of the velocity after each time step. In this article, the number of nonlinear iterations of the Newton–Raphson strategy is used instead.

4 | TIME AVERAGING TECHNIQUE ON NONLINEAR OSCILLATOR

To demonstrate the concept and advantages of the proposed time averaging technique is first applied to the 1D nonlinear oscillator problem

$$M\ddot{u}(t) + C\dot{u}(t) + K(u)u(t) = F, \ u(0) = u_0, \ \dot{u}(0) = v_0 \tag{40}$$

in which u is the displacement, M is the mass, C is the damping coefficient, K is the stiffness and F the external force. The initial displacement u_0 and velocity v_0 are assumed to be given. Defining the velocity v allows to rewrite the second-order ODE in Equation (40) into a system of first-order ODEs as

$$\begin{cases} \dot{v}(t) = \frac{1}{M}(F - Cv(t) - K(u)u(t)) \\ \dot{u}(t) = v(t) \end{cases}. \tag{41}$$

In order to discretize Equation (41) in time, the adaptive time step size BDF2 scheme in Equation (23) is recovered. Hence, the time discrete version of Equation (41) reads

$$\dot{v}_{n+1} = \omega_0 v_{n+1} + \omega_1 v_n + \omega_2 v_{n-1}, \tag{42a}$$

$$\dot{u}_{n+1} = \omega_0 u_{n+1} + \omega_1 u_n + \omega_2 u_{n-1}, \tag{42b}$$

$$u_{n+1} = u_n + v_{n+1}\Delta t_{n+1}, \tag{42c}$$

where ω_0, ω_1 and ω_2 are the adaptive BDF2 coefficients given in Equation (24).

As in Section 2, Equation (42) needs to be rewritten in residual form so that the unknowns u_{n+1} and v_{n+1} can be obtained by iteratively solving a linear system of equations. In this simple case, the discrete in time residual form of Equation (41) is given by

$$\begin{aligned} R_v(u_{n+1}, v_{n+1}) &= F - M\dot{v}_{n+1} - C\dot{u}_{n+1} - K(u_{n+1})u_{n+1} \\ &= F - M\left(\omega_0 v_{n+1} + \omega_1 v_n + \omega_2 v_{n-1}\right) - C\left(\omega_0 u_{n+1} + \omega_1 u_n + \omega_2 u_{n-1}\right) - K(u_{n+1})u_{n+1}, \end{aligned} \tag{43a}$$

$$\begin{aligned} R_u(u_{n+1}, v_{n+1}) &= v_{n+1} - \dot{u}_{n+1} \\ &= v_{n+1} - \left(\omega_0 u_{n+1} + \omega_1 u_n + \omega_2 u_{n-1}\right). \end{aligned} \tag{43b}$$

Hence, the problem is to find u_{n+1} and v_{n+1} such that $R_v(u_{n+1}, v_{n+1}) = 0$ and $R_u(u_{n+1}, v_{n+1}) = 0$. This is achieved by applying the Newton–Raphson method[19] to minimize the residuals in Equation (43). By applying the time averaging technique, we substitute the time instantaneous quantities u_{n+1} and v_{n+1} in Equation (43) by time averaged quantities $\overline{u}_{n+1}$ and $\overline{v}_{n+1}$. Substituting Equation (27) into Equation (42), the new residual functions yield:

$$\begin{aligned} R_v(\overline{u}_{n+1}, \overline{v}_{n+1}) = F - \begin{bmatrix} \omega_0 & \omega_1 & \omega_2 \end{bmatrix}\left(M \begin{bmatrix} \alpha_{n+1}\overline{v}_{n+1} + \beta_{n+1}\overline{v}_n \\ \alpha_n\overline{v}_n + \beta_n\overline{v}_{n-1} \\ \alpha_{n-1}\overline{v}_{n-1} + \beta_{n-1}\overline{v}_{n-2} \end{bmatrix} + C \begin{bmatrix} \alpha_{n+1}\overline{u}_{n+1} + \beta_{n+1}\overline{u}_n \\ \alpha_n\overline{u}_n + \beta_n\overline{u}_{n-1} \\ \alpha_{n-1}\overline{u}_{n-1} + \beta_{n-1}\overline{u}_{n-2} \end{bmatrix} \right) \\ - K(\alpha_{n+1}\overline{u}_{n+1} + \beta_{n+1}\overline{u}_n)(\alpha_{n+1}\overline{u}_{n+1} + \beta_{n+1}\overline{u}_n) \end{aligned} \tag{44a}$$

$$R_u(\overline{u}_{n+1}, \overline{v}_{n+1}) = (\alpha_{n+1}\overline{v}_{n+1} + \beta_{n+1}\overline{v}_n) - \begin{bmatrix} \omega_0 & \omega_1 & \omega_2 \end{bmatrix}\begin{bmatrix} \alpha_{n+1}\overline{u}_{n+1} + \beta_{n+1}\overline{u}_n \\ \alpha_n\overline{u}_n + \beta_n\overline{u}_{n-1} \\ \alpha_{n-1}\overline{u}_{n-1} + \beta_{n-1}\overline{u}_{n-2} \end{bmatrix}, \tag{44b}$$

where α_* and β_* are the time averaging factors computed as described in Equation (29). Then the time averaged quantities $\overline{u}_{n+1}$ and $\overline{v}_{n+1}$ can be solved in the same way as for the time instantaneous ones using a Newton–Raphson iteration. The following parameters are considered for the resolution of the simple nonlinear oscillator:

TABLE 1 Performance of averaging solver compared with the time instantaneous solver

	Temporal iteration	Nonlinear iterations	$u(t = 500\ \text{s})$	$\bar{u}(t = 500\ \text{s})$
Reference solver	50,000	75,659	0.19283	0.189732
Time averaging solver	50,000	75,655	0.19283	0.189732
Accelerated time averaging solver with exponential growth	2455	4267	0.19283	0.189734
Accelerated time averaging solver with linear interpolation	3711	6686	0.19283	0.189752

- $F = 0.2$
- $M = 1$
- $C = 0.15$
- $K(u) = u(t)^2 + 1$
- $u(0) = 1$ and $v(0) = 0$

Four types of solvers are employed for comparison. We refer to the solver that solves Equation (43) as the time instantaneous solver and directly averages its result with Equation (26) as the reference solver. The solver that solves Equation (44) is referred to as the time averaging solver. In addition, two accelerated averaging solvers were considered: one employs the exponential growth method as discussed in Section 3.3.1; the other one employs the linear interpolation method based on the CFL number as discussed in Section 3.3.2. It is to be noted that for this nonlinear spring system, the CFL number stated in Equation (34) does not exist since there is no spatial discretization. Hence, $\Delta x = 1$ is assumed in the calculation of the pseudo-CFL number that is used in the linear interpolation adaptive time step size calculation.

A constant time step size $\Delta t_{\min} = 0.01$ s is set for both the reference solver and the time averaging solver. This value is also used as $t_{\min}$ in both acceleration methods. From previous experience, it is concluded that it is advisable to take at enough sampling points within one period of oscillation. Accordingly, the maximum time step size is set to $\Delta t_{\max} = 0.25$ s for both acceleration methods. For the linear interpolation method, $\text{CFL}_{\min} = 0.001$ and $\text{CFL}_{\min} = 0.01$ are chosen. For the exponential growth method, the time step growth ratio is $r = 1.005$.

The left column of Figure 1 depicts the displacement evolution $u(t)$. Note that, aiming to ease the results visualization, we only zoom in the first 100 s of simulations. Besides, the number of nonlinear iterations per temporal step required to solve Equations (43) and (44) is depicted in the right-hand side of Figure 1. The total Newton–Raphson iterations(nonlinear iterations) are listed in Table 1 together with the total temporal iterations required to reach the steady solution. Final time instantaneous and time averaged displacements are collected as well.

As shown in Figure 1, the four solutions are very similar in terms of both the time instantaneous quantity $u(t)$ and the time averaged quantity $\bar{u}(t)$. It can be also observed that the time instantaneous quantity $u(t)$ of all four solvers converges to the steady state solution $u_s = 0.19283$ at $t = 500$ s. Concerning the computational performance, the accelerated averaging solvers are the most efficient ones as they require the fewest temporal iterations. The same behavior can be noted for the nonlinear Newton–Raphson iterations. All four solvers also show a diminution in the required nonlinear iterations for each temporal step as the simulation evolves, which manifests a reduction of the nonlinearity of the problem.

Comparing the solution of the averaging solver with the reference one shows an almost identical result in both the magnitude and the frequency of time instantaneous and time averaged quantities. This confirms that the solutions of
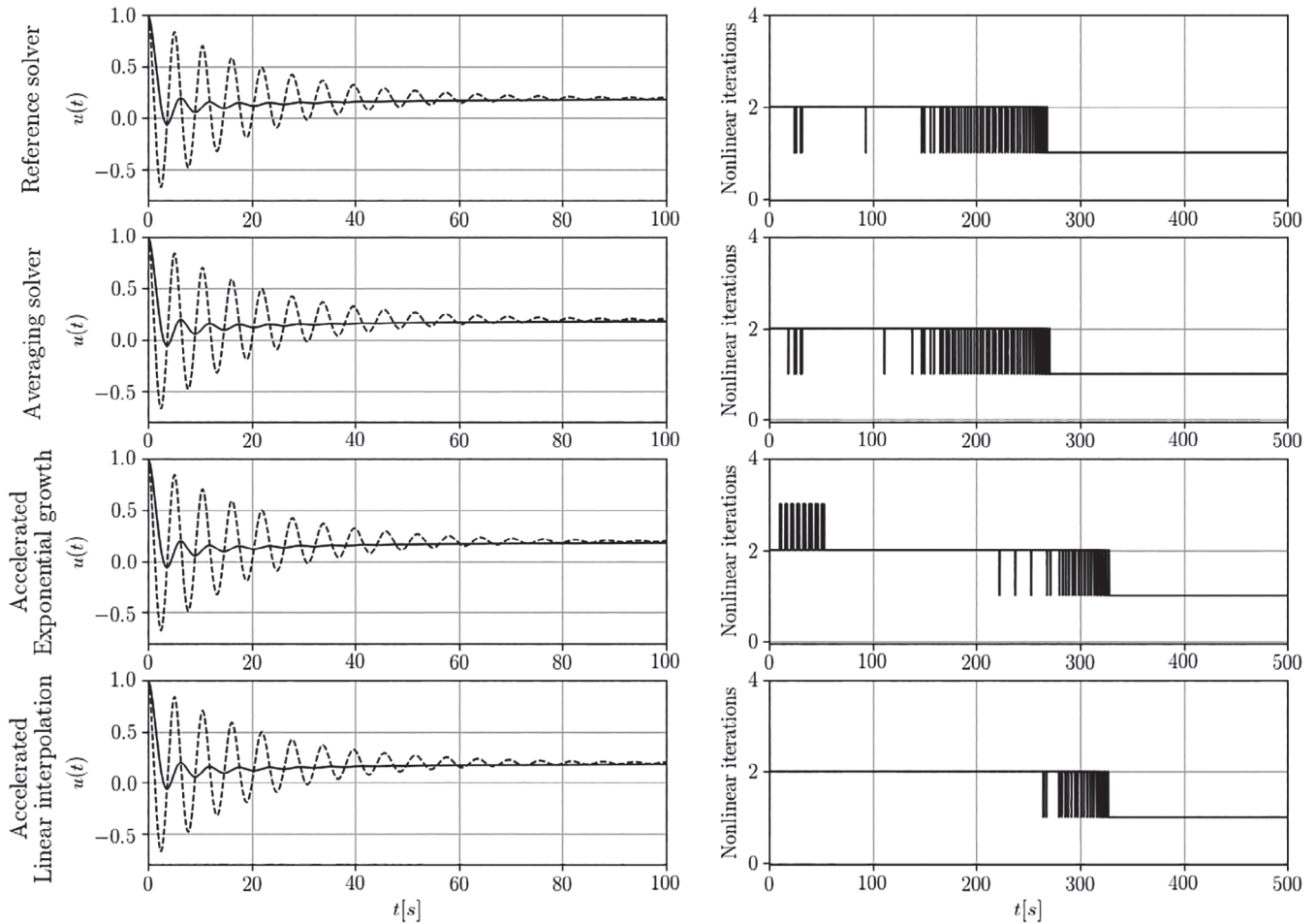
FIGURE 1 A hands-on example of time averaging technique application on a one-dimensional nonlinear spring system. In the left column, the displacements of the spring are plotted from 0 to 100 s. - - - denotes time instantaneous quantity $u(t)$ while — denotes time averaged quantity $\bar{u}(t)$. In the right column, the nonlinear iterations in the Newton–Raphson method are plotted versus the simulation time. Note that the time step sizes of the solvers are different

Equations (25) and (30) are the same. Moreover, the averaging solver took fewer internal nonlinear iterations as the averaged quantities behaved more linearly than the time instantaneous one, as also shown in Table 1. Even though such difference is not apparent in this example, owing to the reasonably small nonlinearity of the problem at hand, this nonlinearity reduction might have a larger impact in the performance of more complex problems as will be shown in Section 5.

Regarding the two acceleration strategies, the obtained results are in general terms in very good agreement with those ones of the reference solver (Figure 1). However, it is also observed the time averaged quantities $\bar{u}(t = 500 \text{ s})$ of the accelerated solvers are slightly higher than those ones of the reference solver (Table 1). This could be associated with the fact that using larger time step sizes introduces additional numerical damping into the system, which reduces the oscillation and thus affects the final time averaged value. Rapidly increasing time step size can also increase the number of nonlinear iterations required in a temporal step, as shown in Figure 1 for the accelerated solver with exponential growth.

When comparing between the two accelerated solvers, the averaging solver with exponential growth gives a more accurate result with fewer nonlinear iterations than the accelerated solver with linear interpolation. One possible explanation for this is that the time step size based on the CFL number is too large at time positions corresponding to zero velocity. Nevertheless, both accelerated solvers show a remarkable acceleration in terms of the nonlinear iterations with little loss of accuracy.

It is worthwhile noting that the choice of the acceleration parameters is a trade-off between accuracy and efficiency. In this regard, it must be clearly stated that even though a fast acceleration speeds up the simulation it might also introduce

numerical error to the system. Hence, a thorough selection of problem-dependent acceleration parameters is required and is out of the scope of this work.

In conclusion, it can be said that this simple example proves the validity of the proposed time averaging technique based on the reduction of the nonlinearity, which makes possible to increase time step size. In the following chapter, the same technique is applied to turbulent flow problems, whose nonlinearity, and thus complexity, are inherently larger than that one of the current example.

5 | RESULTS AND DISCUSSION

In the following, three test cases will be presented and compared with experimental results and numerical results from other researchers. The directly time averaged result obtained from the instantaneous solver based on the same VMS formulation is employed as a reference. Acceleration and stabilization are also taken into account in the numerical investigation. The two-dimensional (2D) BFS case is analyzed in details, whereby the convergence to the steady state and the acceleration methods will be presented. In the other two cases, the averaging solver is briefly validated against the reference solver and the experimental results. For all cases where time averaging solver is mentioned without specifying the time step size acceleration method, the exponential growth approach with a growth ratio of 1.05 is employed. All the simulations are performed sequentially with an Intel Core i7-7700HQ CPU @2.80 GHz processor.

5.1 | 2D backward facing step

The flow over a BFS is a simple canonical flow that shows both separation and reattachment and has been extensively investigated both experimentally and numerically (e.g., Kim & Moin,[20] Sohn,[21] Gartling,[22] Gresho et al.[23]) and often serves as a benchmark problem for numerical codes. This 2D BFS test case is derived directly from the experiment by Armaly et al.[24] In the experiment, velocity distribution and reattachment lengths are measured for different Reynolds numbers. In the following section, the numerical results are validated with the experimental results.

5.1.1 | Experimental setup

With a high aspect ratio of the experimental test section, the flow is considered fully developed and 2D. Nevertheless, the experimental results indicated that the downstream step remained 2D only at low Reynolds numbers. In the experiment, results for laminar, transient and turbulent airflow in a Reynolds number in the range of $70 < Re < 8000$ are presented. In the following, numerical results for different Reynolds numbers from all three flow regimes are compared with the experimental results.

- $Re < 1200$: laminar, 2D flow
- $1200 < Re < 6600$: transitional, strong, 3D flow
- $Re > 6600$: turbulent, strong, 3D flow

In addition, an expansion ratio of 1:1.94 of the inlet channel height and the channel height with a step height of 5.2 cm is considered in the experiment. It is stated by Armaly et al.[24] and also in other articles[25,26] that the expansion ration has an influence on the reattachment length of the primary separation region, especially with turbulent flows. Therefore, the exact expansion ration and the step height are strictly kept in the numerical investigation.

The stability of the steady, incompressible 2D flow over a BFS has been studied by many researchers. Fortin et al.[27] show that the 2D flow is stable over a BFS close to the Reynolds number of 1600. Barkley et al.[28] restrict this number to 1050 for linear stability to 2D perturbations. Alongside with the three-dimensionality, flows with a high Reynolds number present unsteady large-scale structures. Previous research on the BFS flow of, for example, Abe et al.,[29] Craft,[30]
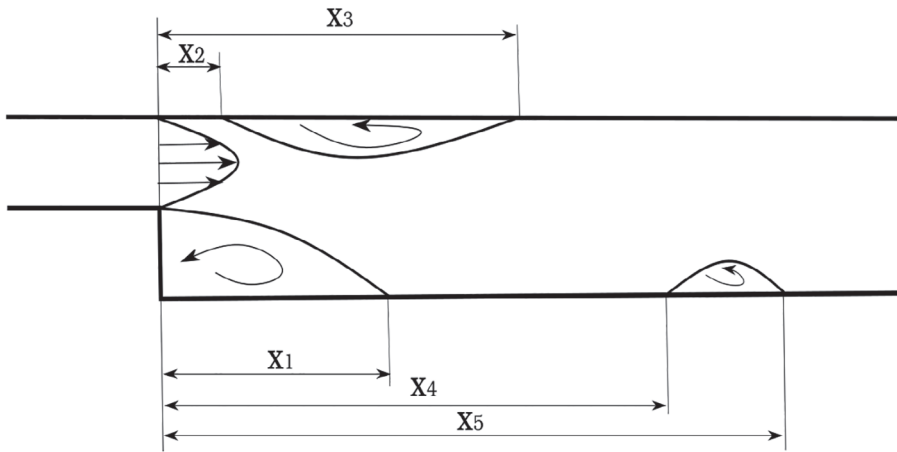
FIGURE 2 Location of detachment and reattachment of the backward facing step flow

and Parneix et al.[31] with steady RANS formulation has shown difficulties in reproducing the main characteristics of the flow such as recirculation length, backflow intensity and boundary-layer recovery. Despite the unsteadiness, there are well-defined time averaged mean separation bubbles that are often observed in experiments and are also used in this article to demonstrate the accuracy of the solvers. The locations of these separation bubbles are noted by detachments and reattachments of the BFS flow, which are illustrated schematically in Figure 2. The primary reattachment length, denoted as x_1, exists for all Reynolds numbers. As the Reynolds number increases, the second recirculation zone, the length of which is indicated by x_4 and x_5, starts to appear at Re > 400. As the Reynolds number further increases, the third recirculation zone, indicated by x_2 and x_3, appears on the upper wall and remains in the Reynolds number range of 1200 < Re < 2300. As the Reynolds number continues to increases and the flow becomes more turbulent, both the second and the third recirculation zones vanish.

The flow state under the four cases considered in the numerical investigation are summarized below:

- Re = 100: laminar flow, only primary recirculation zone
- Re = 1290: transitional flow, primary as well as secondary recirculation zone on the lower wall
- Re = 1880: transitional flow, primary as well as secondary recirculation zones on the upper and lower wall
- Re = 6600: turbulent flow, only primary recirculation zone

For all Reynolds numbers, a fully developed parabolic flow is obtained at the inlet boundary, see in Figure C4 in the Appendix. However, at the outlet boundary, the flow is not fully developed for the fully turbulent flow with Re = 6600, which indicates that the domain is not large enough. Therefore, the outlet boundary is further replaced by 200 h in the downstream direction for the Re = 6600 case.

5.1.2 | Numerical setup

The numerical setup does not have an identical physical setup as in the experiment. It is set up in such a way that the inlet and outlet boundary conditions yield nominally 2D flow, the schematic of the numerical setup is to be found in Figure 3.

- Inlet boundary condition:
  At the inlet boundary condition, a poiseuille flow is considered. Air is the working fluid. The mean inflow velocity is calculated from the Reynolds number, which is defined as:

$$\text{Re} = \frac{\bar{u} \cdot 2h_i}{\nu}. \tag{45}$$

Selecting the position of the step as the origin, the inflow velocity is a parabolic function of the y-coordinate, given as:
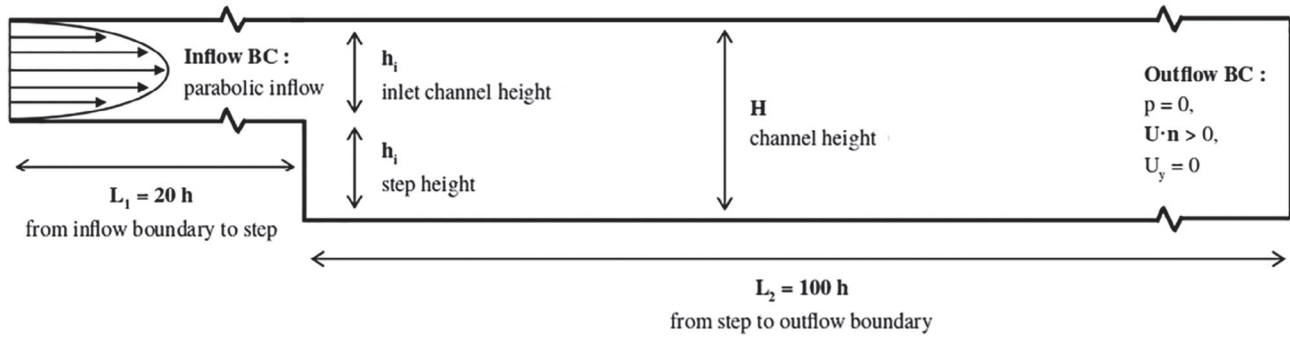
FIGURE 3 Numerical setup of the experimental reproduction of two-dimensional flow over a backward facing step

$$u(y) = u_{\max} \left(1 - \left(\frac{y - (h + h_i/2)}{(h_i/2)} \right)^2 \right), \tag{46}$$

where $u_{\max} = 1.5 \cdot \bar{u}$ for a poiseuille flow.

- Outlet boundary condition:

  The outlet boundary is located at a distance of 100 h downstream of the step. The pressure is set to a constant value of $p = 0$. In addition, to prevent backflow at the outlet boundary, the outflow direction is set to be perpendicular to the outlet boundary and pointing outwards.

- Wall boundary condition:

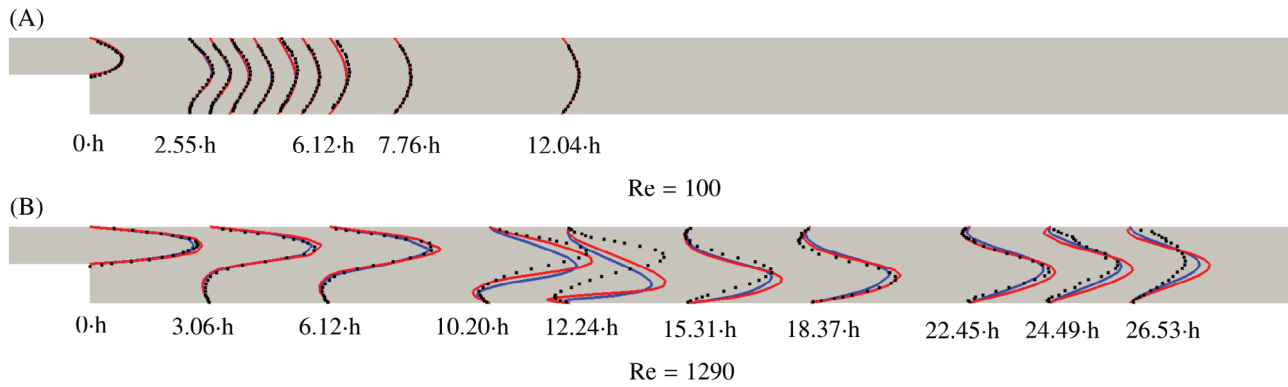 Nonslip boundary conditions are applied to all of the channel walls.

- Initial boundary condition:

  The averaging solver is very sensitive to any extreme values. In the initial step, extremely large pressure dominates the computational domain and drives the initial zero velocity, which causes the averaging solver a large number of extra iterations to compensate for this effect. Therefore, the averaging solver uses the solution of the instantaneous solver after some iterations as the initial condition to avoid this phenomenon.

It should be noted that the locations of the inlet and outlet boundaries play a critical role. This is noticed by Erturk[32] in his simulations based on the same experiments that fully developed flow cannot be acquired without a sufficiently long inlet and outlet buffer domain, which lead to a violation of the boundary conditions. We note that for Re < 1000, a downstream length of 100 h is sufficient, and for 1000 < Re < 3000, a greater downstream length of 300 h is required. All grids are created by the pre and post processor GiD.[33] The detailed mesh configuration can be found in Figures B1 and C1 in the Appendix. The smaller domain contains 43k elements, while the larger domain contained 101k elements.

5.1.3 | Validity of the reference solver

To validate the results of the reference solver and the averaging solver, the velocity profiles at different positions are compared with the experimental results of Armaly et al.[24] For the available datasets of Re = 100 and Re = 1290, the results are presented in Figure 4. For Re = 100, the results of the reference solver and the time averaging solver are consistent with the experimental results, while for Re = 1290, a good overall agreement is shown, except for the velocity profiles at $x = 12.24$ h. These differences can be explained by the early prediction of the reattachment position x_1 at $x = 15.32$ h as listed in Table 2 by the numerical solvers. Nevertheless, the results from the time averaging solver are always consistent with the reference solver. As described by Armaly et al.[24] in his article, the flow between 400 < Re < 6600 is fully 3D. The disagreement of the velocity profiles observed at far downstream locations is probably caused by the 3D effects. This effect is also observed by Erturk[32] in their article, though their disagreement with the experimental results appeared at further downstream locations. Apart from this slight discordance, the result is a confirmation of the accuracy of both reference solver and the time averaging solver. For higher Reynolds numbers, no experimental results are available. The results of the time averaging solver are validated against the reference solver.

(A)

0·h   2.55·h   6.12·h 7.76·h   12.04·h

Re = 100

(B)

0·h   3.06·h   6.12·h   10.20·h 12.24·h   15.31·h   18.37·h   22.45·h 24.49·h 26.53·h

Re = 1290

FIGURE 4 Comparison of velocity profiles at various locations, where red ▬ presents the result of the averaging solver; blue ▬ presents the directly averaged result; … … presents the experimental result from Armaly et al. [Color figure can be viewed at wileyonlinelibrary.com]

TABLE 2 Detachment and reattachment locations normalized with step height h at various Reynolds numbers with experimental result from Armaly et al.[24] and numerical results from References 32 and 34

		x_1	x_2	x_3	x_4	x_5
Re = 100	Experiment Armaly	3.08	–	–	–	–
	Erturk	2.92	–	–	–	–
	Biswas et al.	2.71	–	–	–	–
	Reference solver	2.85	–	–	–	–
Re = 1290	Experiment Armaly	15.32	11.39	22.63	–	–
	Erturk	14.86	11.92	30.86	–	–
	Reference solver	12.78	10.49	25.89	–	–
Re = 1880	Experiment Armaly	15.32	11.39	22.63	19.94	23.19
	Erturk	17.87	14.45	39.24	36.65	46.98
	Reference solver	14.52	12.37	32.22	32.42	39.23
Re = 6600	Experiment Armaly	8.00	–	–	–	–
	Reference solver	20.32	14.84	34.64	31.50	33.73

Table 2 shows the detachment and reattachment positions normalized by the step height obtained by the reference solver and other researchers' numerical or experimental methods.

In the laminar region, a very well coincidence between the reference solvers and the experimental results is obtained, with an error le 7.5%. This is in a good agreement with the numerical result of Erturk[32] as well as results of Biswas et al.[34] Although Erturk[32] have a smaller error comparing to the present result, it must be taken into account that the number of grids used in the present article is about an order of magnitude smaller than the number of grids used in Erturk.[32]

In the transitional region, a stable, steady solution is obtained, however, due to the limitation of 2D flow simulation, the presented results do not align as well as in the laminar case with the experimental results. Despite a good prediction of the primary recirculation location, the predictions of the secondary recirculation zones at the upper and lower walls are relatively poor, in both terms of location and length. However, as mentioned earlier, this difference may be due to the 3D and unsteady effects of the flow in the transitional region. Other researchers have observed similar results in their 2D flow simulations that the recirculation length cannot be captured correctly.[34,35] Erturk[32] have similar reattachment lengths in their article for Re = 1900 for a BFS flow with an expansion ratio of 1 : 2. Furthermore, Armaly et al.[24] also note in their experiment that the flow is fully 3D in the transitional region. In the fully turbulent flow region, the instantaneous solver does not yield a steady state solution, and the disagreement between the reference solver and the experimental results is evident. Another factor that cannot be neglected for the lack of accuracy is that the grid used in the article is relatively coarse (around 40,000 elements) compared with all the other present articles. For instance, Erturk[32] had a mesh

with 300,000 elements. For even higher Reynolds numbers in the turbulent region, there are no other available numerical simulation results with 2D analysis.

In the turbulent region, the flow is fully unstable and unsteady. There are hardly any numerical investigations in 2D for BFS in with a high Reynolds number. Reasonable numerical results available are all conducted in 3D and even partially with DNS. Due to the computational limit, a 3D simulation is not feasible within this project. As expected, the result of the reference solver presents a large discrepancy to the experiment due to an oscillating behavior of downstream of the step from the time instantaneous solver. This instability is also present in the averaging solver, the result of which will be discussed later in this section. The result of the averaging solver for the turbulent region will only be validated against the direct average of the instantaneous solver.

### 5.1.4 | Examination of the convergence to the steady state

Before the results are further validated with the experimental results based on the detachment and reattachment locations, the steadiness of the flows should be first determined. As defined in Section 3.2, the quasi steady state is reached when the temporal changes of time averaged quantities over the time step falls below a tolerance value. Here, the rates of change of velocity magnitude and pressure are normalized by the free-stream velocity magnitude and the dynamic pressure, respectively, so as to nondimensionalize the problem. The steady state convergence is monitored by these two quantities. As shown in Figure 5, a clear convergence to the steady state of both the reference solver and the averaging solver is observed for all Reynolds number flows. Note that Figure 5 represents the relative change of the velocity and pressure magnitude, not the residual of these quantities. For Re = 6600, it can be observed that all three methods no longer change much after 1 s, there is no need to run for such a long time window.

The averaging solver without time step size acceleration achieves a very similar rate of convergence as the time averaging of the time instantaneous result for all Reynolds numbers. It should be noted here that the convergence refers to the convergence to the steady state instead of the residual convergence. The averaging solver with acceleration outer-performs the other two solvers in the sense that it has the fastest rate of convergence to the steady state. The averaging solver starts with a fast convergence in the beginning, and then the convergence slows down and reaches a similar rate of convergence as the reference solver. As the Reynolds number increases, the differences between averaging solvers with and without acceleration becomes milder; the normalized rate of change of the velocity magnitude remains smooth whereas the rate of change of pressure exhibits an oscillating behavior. This is the main reason that only the normalized rate of change of the velocity magnitude is used as the measure for steady state convergence instead of using both. Choosing $1e - 3$ as the tolerance for the normalized rate of change of the speed magnitude and the stop criteria for analyzing the efficiency of different solvers, the numbers of total temporal iterations required for the three solvers are listed in Table 3. As can also be seen in Figure 5, the numbers of iterations required by the reference solver and the averaging solver are very close. However, since the criterion of constant CFL number is applied for both the reference and the averaging solvers and the latter is in the procession of smaller nodal extreme velocity magnitudes, the time step sizes of the averaging solver are in comparison to those of the reference solver larger, leading to less required iterations. Furthermore, since the averaged NS equations are better conditioned, fewer nonlinear iterations are required within a temporal iteration. Thus, the time elapsed for the averaging solver is considerably reduced compared with that of the reference solver. One remark on the iterations required is that stabilization is applied in the case of Re = 6600 but not in the other three cases, slowing down the rate of convergence to the steady state.

Further from Table 3, a clear acceleration to the steady state of the accelerated averaging solver can be observed. In the laminar case, the accelerated averaging solver needs only 18.5% of the solving time of the reference solver. In the transitional cases, the accelerated averaging solver outperforms the reference solver even better with only ≈3.5% of the solving time of the reference solver. In the fully turbulent case, the accelerated averaging solver outperforms the reference solver with only 8.0% of its solving time despite a slowdown due to the instability.

5.1.5 | Examination of the averaging solver

As mentioned before, the accuracy of the averaging solver is highly related to the accuracy of the reference solver as they are solved with the same computational grid and the same discretization method. Due to the two-dimensionality
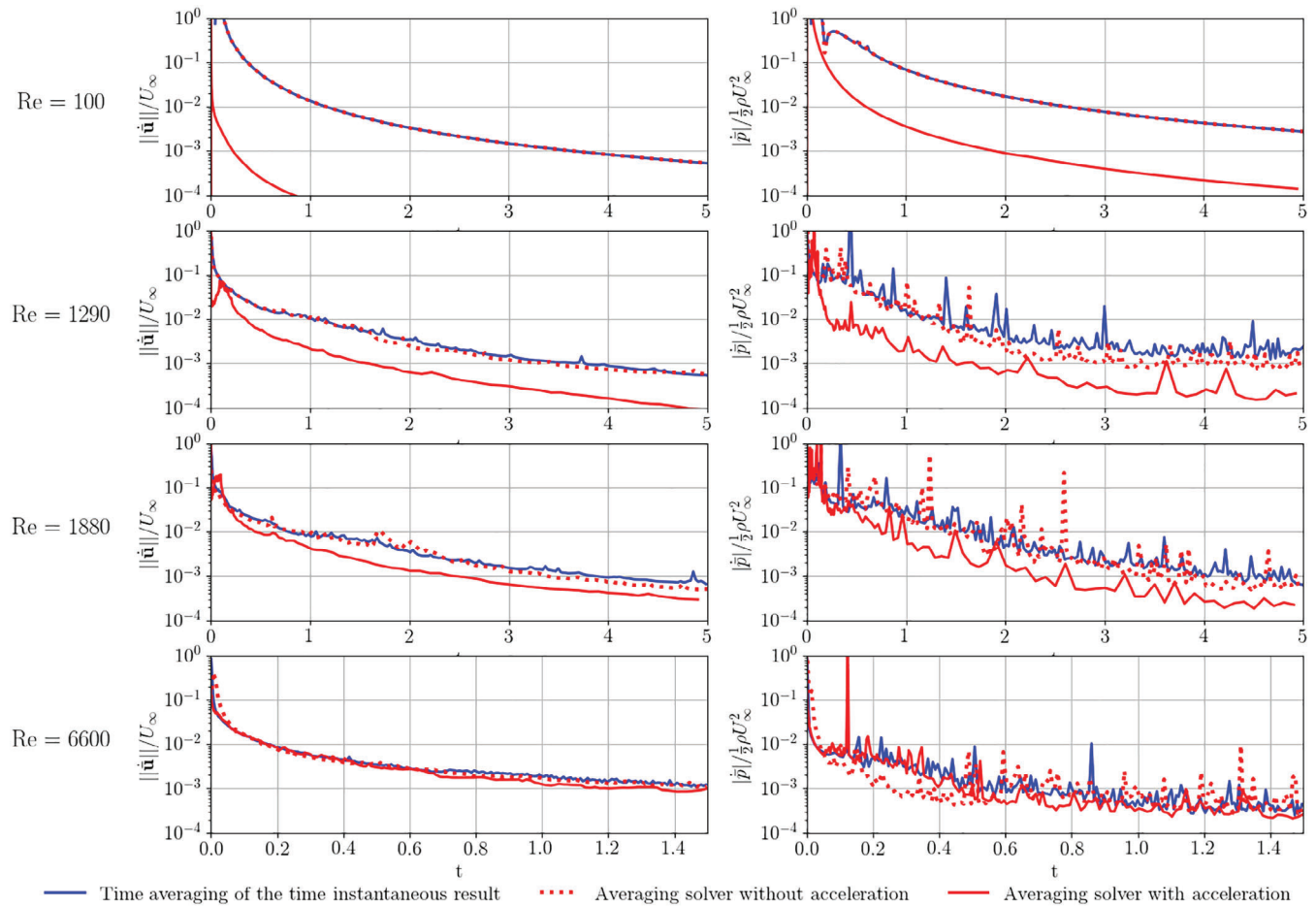
FIGURE 5 Steady state convergence monitored by the normalized rate of change of velocity magnitude and pressure [Color figure can be viewed at wileyonlinelibrary.com]

and computer resource limitations, without loss of generality, the presented solver will now only be compared with the reference solver. Figure 6 presents the streamlines derived with the reference solver and the averaging solver for all Reynolds numbers. Their results are compared and tabulated in Table 4. For each Reynolds number case, the results are analyzed at $t = 5$ s, except for Re $= 6600$, in which case the result is analyzed at $t = 0.8$ s. The streamlines derived from the instantaneous solver, the direct averaging of the instantaneous results and the averaging solver are hardly distinguishable. The exact detachment and reattachment positions are to be found in Table 2. As shown in Figure 6, the detachment and reattachment locations of the reference solvers and the averaging solvers lie close to each other. Comparing the averaging solver and the reference solver, the overall error falls within 5%. In general, the relative error of the accelerated averaging solver shares the same magnitude of relative error with the nonaccelerated averaging solver, except for the case in the turbulent region with Re $= 6600$.

On closer inspection of results of the high Reynolds number case Re $= 6600$ in Figure 6, the instantaneous solver provides a solution with a clear oscillation at a distance of approximately 33 h in the downstream direction as the flow became fully turbulent. The directly averaged result succeeded in delivering a steady state solution, which is consistent with the result derived from the averaging solver (Figures 7 and 8). It is worth mentioning that due to the unsteadiness inherently in the time instantaneous problem, the acceleration of the averaging solver for Re $= 6600$ requires a stabilization as described in Section 3.4. The acceleration and stabilization of the averaging solver for Re $= 6600$ will be further explained in the following section. The directly averaged result succeeded in delivering a steady state solution, which is consistent with the result derived from the averaging solver. It is worth mentioning that due to the unsteadiness inherently in the time instantaneous problem, the acceleration of the averaging solver for Re $= 6600$ requires a stabilization as described in Section 3.4. The acceleration and stabilization of the averaging solver for Re $= 6600$ will be further explained in the following section.

TABLE 3 Iterations needed for each solver to achieve $||\dot{\bar{u}}|| < 1e-3$

		Temporal iterations	Elapsed time
Re = 100	Reference solver	541	439 s
	Averaging solver	492	265 s
	Accelerated averaging solver	95	81 s
Re = 1290	Reference solver	7863	668 m
	Averaging solver	7097	478m
	Accelerated averaging solver	182	25 m
Re = 1880	Reference solver	9501	1201 m
	Averaging solver	9206	724 m
	Accelerated averaging solver	238	39 m
Re = 6600	Reference solver	21,934	5934 m
	Averaging solver	19,423	1259 m
	Accelerated averaging solver	4382	476 m

TABLE 4 Error estimation with respect to the reference solver

		x_1	x_2	x_3	x_4	x_5
Re = 100	Reference solver	2.85	–	–	–	–
	Averaging solver	2.84 (−0.3%)	–	–	–	–
	Accelerated averaging solver	2.84 (−0.3%)	–	–	–	–
Re = 1290	Reference solver	12.78	10.49	25.89	–	–
	Averaging solver	12.24 (−4.2%)	10.25 (−2.3%)	25.08 (−3.1%)	–	–
	Accelerated averaging solver	12.59 (−1.5%)	10.42 (−0.7%)	26.27 (−1.5%)	–	–
Re = 1880	Reference solver	14.52	12.37	32.22	32.42	39.23
	Averaging solver	14.29 (−1.6%)	12.46 (+0.7%)	32.58 (1.1%)	30.93 (−4.6%)	40.15 (+2.3%)
	Accelerated averaging solver	15.01 (−3.4%)	12.35 (−0.16%)	33.26 (−2.0%)	31.56 (−2.6%)	39.65 (+1.7%)
Re = 6600	Reference solver	20.32	14.84	34.64	31.50	33.73
	Averaging solver	20.69 (+1.8%)	15.01 (+1.14%)	35.19 (+1.6%)	31.88 (+1.8%)	34.15 (+1.2%)
	Accelerated averaging solver	26.10 (+28.4%)	21.22 (+43.0%)	39.34 (+13.5%)	34.78 (+9.92%)	43.74 (+29.6%)

5.1.6 | Stabilization for the turbulent case Re = 6600

For the case with a high Reynolds number Re = 6600, the instantaneous solver encounters a periodic perturbation as the flow becomes very turbulent, leading to difficulties in reaching a steady state. As shown in Figure 9, the instability starts right behind the primary circulation zone. The flow behind the step exhibits a clear periodic oscillation which is carried further in the downstream direction. This oscillation is not damped in time. Corresponding to this oscillating behavior, the time averaged image of the time instantaneous solution shows the separation bubbles in a time averaged sense. The separation points move further downstream as the flow developed. The solution from the averaging solver without acceleration shows almost identical snapshots at all-time snaps compared with the reference solver. A different image occurs when the averaging solver is accelerated. As shown in Figure 9, the accelerated averaging solver already exhibits some sort of oscillating behavior at the initial step. Though this oscillating behavior is damped out in time, it still leads to much larger artificial separation zones. It is worth mentioning that due to an aggressive acceleration strategy, at the time when the accelerated averaging solver reached the same physical time, only one 1.87% of nonlinear iterations are required compared with the nonaccelerated averaging solver.
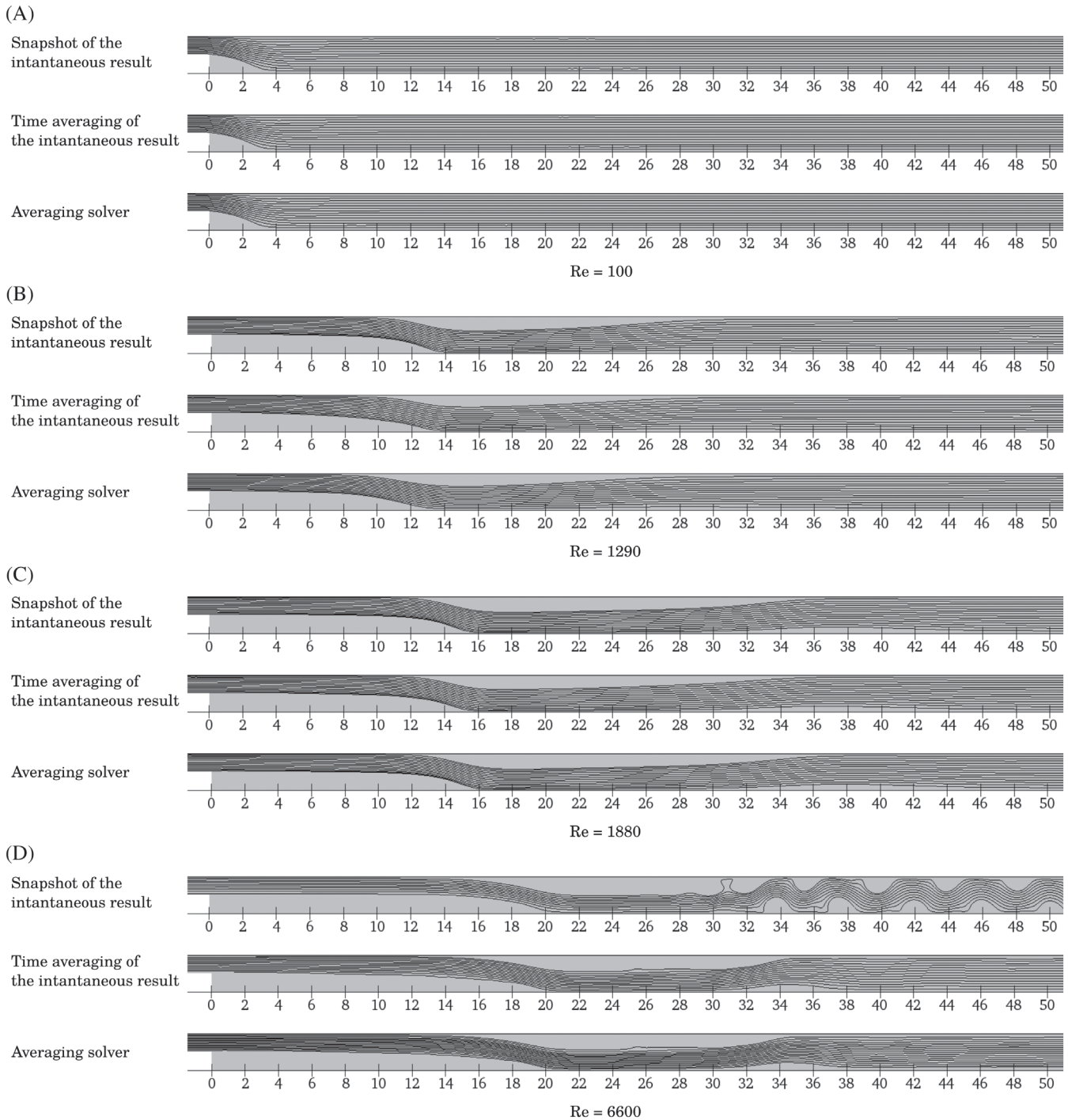
(A)

Snapshot of the
intantaneous result

Time averaging of
the intantaneous result

Averaging solver

Re = 100

(B)

Snapshot of the
intantaneous result

Time averaging of
the intantaneous result

Averaging solver

Re = 1290

(C)

Snapshot of the
intantaneous result

Time averaging of
the intantaneous result

Averaging solver

Re = 1880

(D)

Snapshot of the
intantaneous result

Time averaging of
the intantaneous result

Averaging solver

Re = 6600

FIGURE 6 Streamlines derived with different solvers of different Reynolds numbers

To stabilize the problem caused by the aggressive time step acceleration, the approach described in Section 3.4 is employed. The time step sizes and the number of nonlinear iterations within each time step taken by different solvers versus physical time are plotted in Figure 7. Because the flow solved by the instantaneous solver exhibits an oscillating behavior, the time step size calculated based on the constant CFL number criterion also presents a periodicity. On average, a temporal iteration takes approximately five to six iterations by the instantaneous solver with an averaged time step size of 40 ms. The time step size taken by the exponentially accelerated averaging solver increases almost strictly linearly with respect to the physical time. Its final time step size is increased by two magnitudes compared with the time instantaneous solver. Although the time step size increases, the number of nonlinear iterations within a temporal step also increases
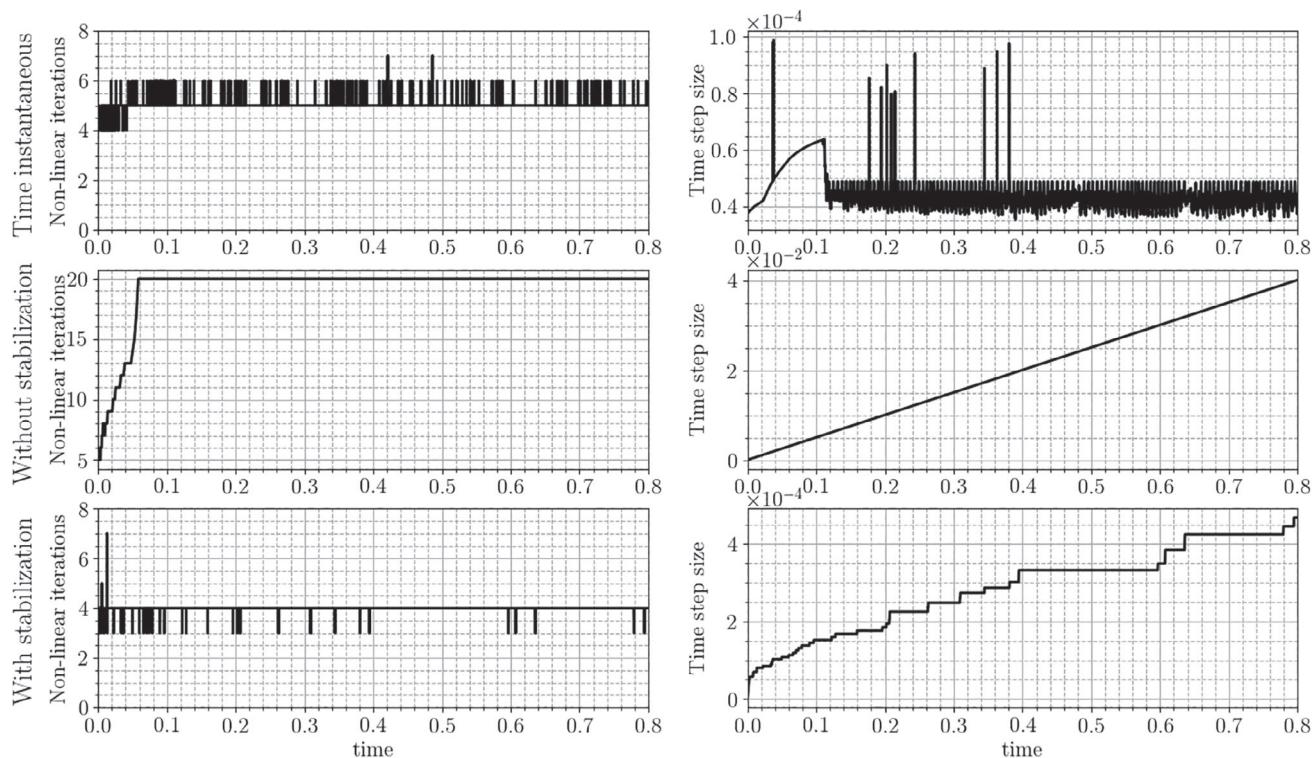
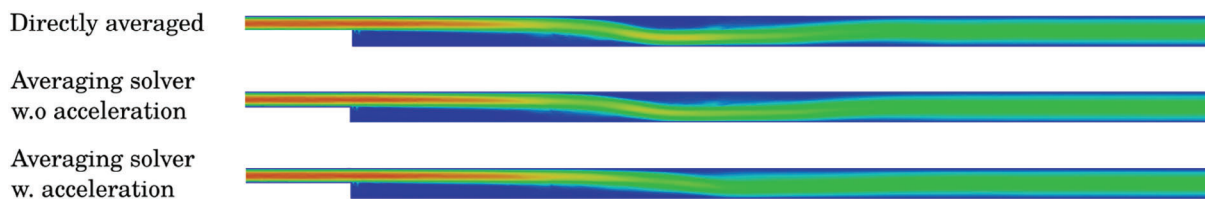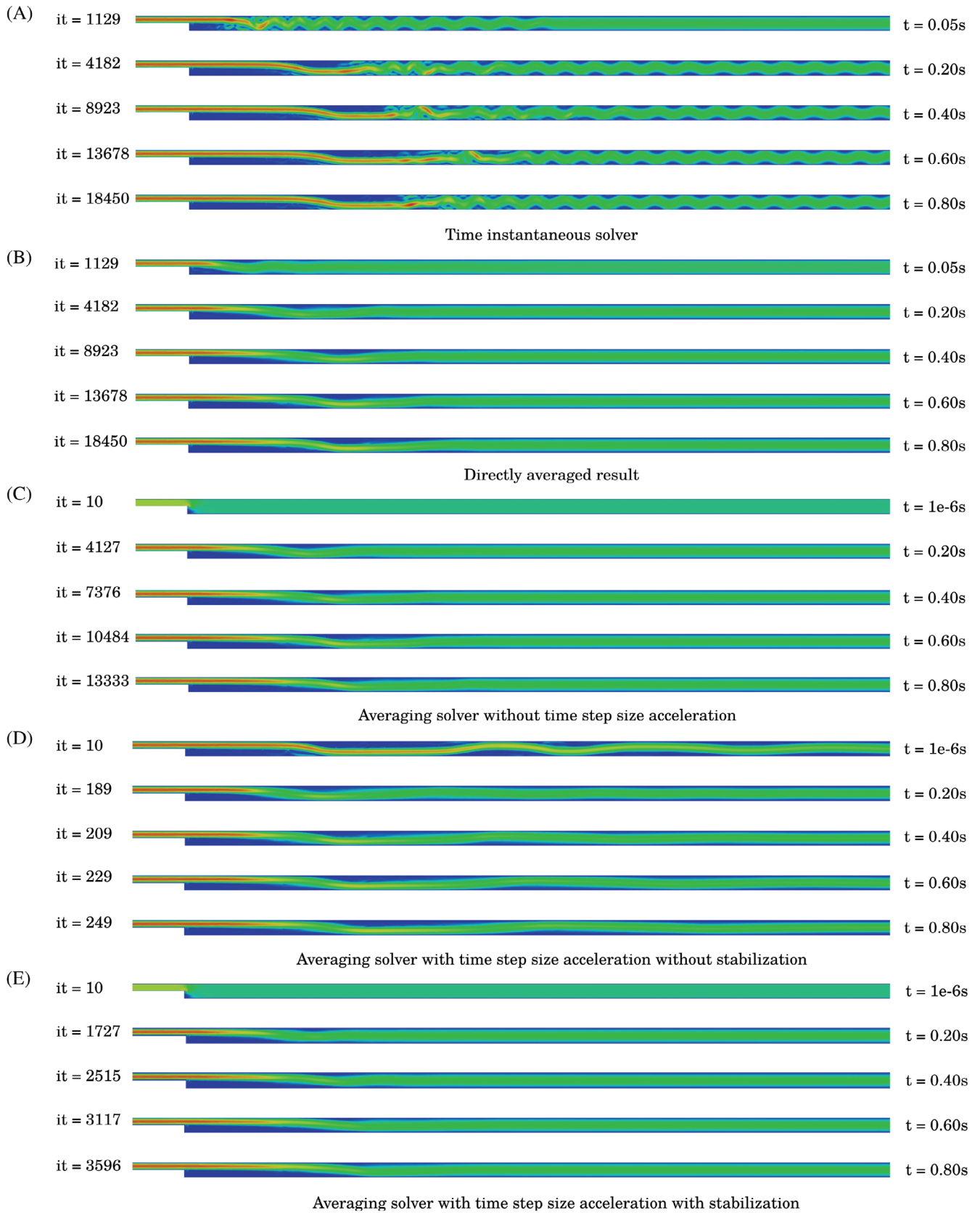**FIGURE 7** Time step size and nonlinear iteration number of case Re = 6600

FIGURE 8 Velocity contour plot of reference solvers for Re = 6600. Reference directly averaged solution is compared with the averaging solver without (w.o) and with acceleration (w.) [Color figure can be viewed at wileyonlinelibrary.com]

and stops increasing after it reached a predefined maximum number of iterations. These insufficient nonlinear iterations within a temporal step resulted in an inaccurate result.

To solve this problem, only temporal iterations without an intense nonlinearity are accelerated; otherwise, the time step size remains the same. With this stabilized acceleration, the averaged number of nonlinear iteration within each temporal step is reduced due to the time averaging formulation, as was shown previously in the nonlinear oscillator example in Section3. With the stabilized acceleration method, the final time step size is increased by a factor of 4. As listed in Figure 9, the accelerated averaging solver with stabilization needs approximately one fifth nonlinear iterations of that of time instantaneous solver and one fourth of that of the averaging solver without acceleration. The zoomed in velocity plot of the averaging solver with stabilization compared with the reference solver and the averaging solver without acceleration is shown in Figure 8. Although the accelerated averaging solver still overpredicts the primary separation zone, the flow no longer exhibits a nonexistent separation bubble, as does the accelerated averaging solver without stabilization.

5.1.7 | Acceleration method

All the results by the accelerated averaging solver presented in the previous sections adapt a constant exponential growth ratio. In this section, the two time step size acceleration approaches discussed in Section3 will be investigated and

(A)

it = 1129   t = 0.05s

it = 4182   t = 0.20s

it = 8923   t = 0.40s

it = 13678   t = 0.60s

it = 18450   t = 0.80s

Time instantaneous solver

(B)

it = 1129   t = 0.05s

it = 4182   t = 0.20s

it = 8923   t = 0.40s

it = 13678   t = 0.60s

it = 18450   t = 0.80s

Directly averaged result

(C)

it = 10   t = 1e-6s

it = 4127   t = 0.20s

it = 7376   t = 0.40s

it = 10484   t = 0.60s

it = 13333   t = 0.80s

Averaging solver without time step size acceleration

(D)

it = 10   t = 1e-6s

it = 189   t = 0.20s

it = 209   t = 0.40s

it = 229   t = 0.60s

it = 249   t = 0.80s

Averaging solver with time step size acceleration without stabilization

(E)

it = 10   t = 1e-6s

it = 1727   t = 0.20s

it = 2515   t = 0.40s

it = 3117   t = 0.60s

it = 3596   t = 0.80s

Averaging solver with time step size acceleration with stabilization

FIGURE 9   Snap shot of velocity contour plot by different solvers for Re = 6600. Note the iteration numbers are the total nonlinear iteration numbers within each temporal step [Color figure can be viewed at wileyonlinelibrary.com]
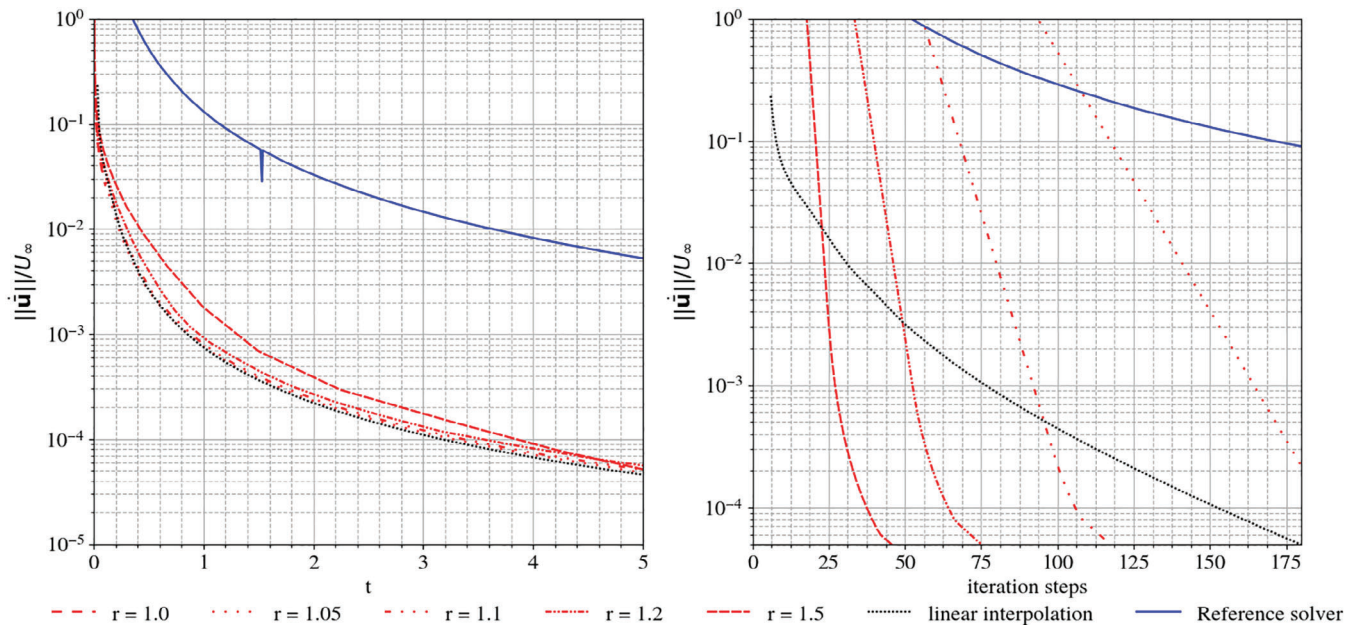
FIGURE 10 Study of time step size acceleration for Re = 100 [Color figure can be viewed at wileyonlinelibrary.com]

analyzed. Several growth ratios are considered for the exponential growth approach. Only Re = 100 is considered and the results are presented in Figure 10. The choice of the growth ratio is based on Becker, who has proven that for PDEs, the numerical stability for the BDF2 scheme is guaranteed for a growth ratio of less than $\frac{2+\sqrt{13}}{3} \approx 1.86$.[36] For all the growth ratios, the same maximum time step size is considered.

The result shows a positive correlation between the growth ratio and the rate of convergence. At the end of the simulation time, a very similar level of convergence with different acceleration strategies is achieved. It is also worth mentioning that all the accelerated averaging solvers show in general a better rate of convergence than that of the reference solver. Nevertheless, with a larger growth ratio, the number of temporal iterations required to reach the same level of convergence is reduced. Comparing the linear interpolation acceleration method with the exponential growth acceleration method, though the former has a slightly better rate of convergence, the latter requires much fewer iteration steps and is thus much more efficient.

Therefore, the exponential growth approach generally outperforms the linear interpolation method and will be applied in the remaining simulations where the accelerated averaging solver is mentioned.

5.2 | 2D forward–backward facing step

The 2D forward–backward facing step (FBFS) test case is derived from an experimental investigation by Leclercq et al.,[37] in which a 2D flow passing a rectangular block on a flat plate is examined. This well-known turbulent flow is examined in this article to validate the robustness and accuracy of the presented averaging solver with high unsteadiness.

5.2.1 | Experimental setup

The experiment is carried out under a Reynolds number of Re = $1.7 \cdot 10^5$. A length-of-height ratio of $L/h = 10$ and an aspect ratio of $L_s/h = 10$ are considered. This configuration ensures a 2D flow in the plane of symmetry.[38] The experiment consists of a boundary layer flow with a thickness of $\delta = 0.8\,h$ and a free stream velocity of $U_0 = 50$ m/s over an aluminum plate with a height of $h = 0.05$ m and a length of $L_s = 0.5$ m. A detailed sketch of the experimental setup is to be found in Figure 11. An important remark on the experiment is that the upper boundary of the air tunnel is streamline-shaped to
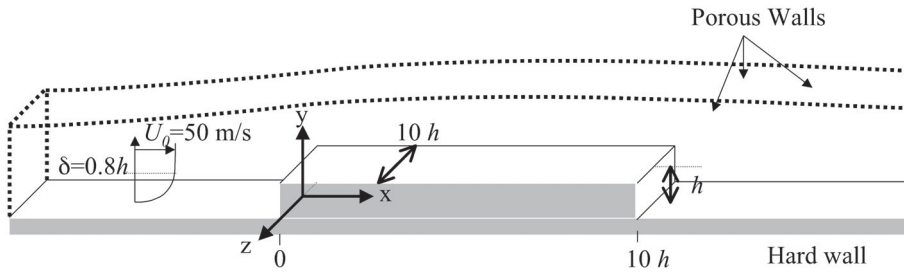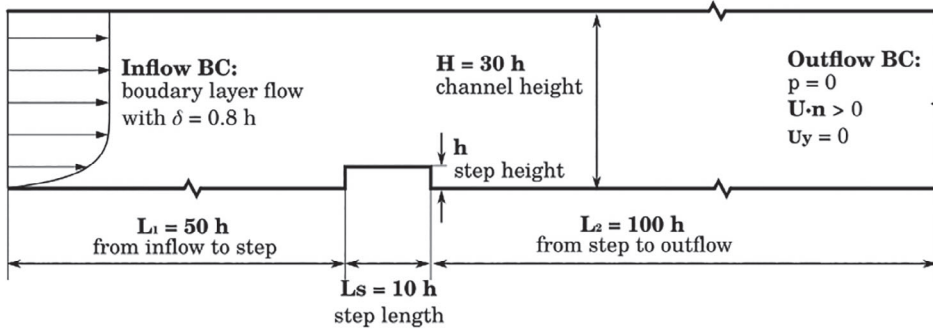
prevent additional pressure gradients under consideration of reasonable design cost. In the numerical setup, a different approach is taken to achieve this.

5.2.2 | Numerical setup

The numerical setup tries to reproduce a wind tunnel experiment. Instead of defining a streamlined wall boundary, the computational domain is considerably large so that both the farfield and the pressure outlet boundary conditions can be fulfilled. The schematic of the numerical setup is to be found in Figure 12.

- Inlet boundary condition:

Air is the working fluid. To model the turbulent boundary layer flow, a velocity profile with power law is employed at the inlet boundary. A velocity profile with a power law is employed at the inlet boundary to model the turbulent boundary layer flow. The velocity profile of Schlichting[39] and Duncan et al.[40] is applied, which can be expressed as:

$$\frac{u}{U_0} = \left(\frac{y}{\delta}\right)^\alpha,$$ (47)

where U_0 is the free-stream velocity. The constant α is adopted from the momentum integral method and $\alpha = 1/7$ is taken in this article as it has a good agreement with experimental data for pipe flows under $\text{Re} < 6 \cdot 10^6$.[41] Considering a boundary layer thickness of $\delta = 0.8$ h and a freestream velocity of $U_0 = 50$ m/s, the inlet velocity profile can be expressed as:

$$u(y) = \begin{cases} U_0 \cdot \left(\frac{y}{\delta}\right)^{1/7} & y \leq \delta \\ U_0 & y > \delta \end{cases}$$ (48)

- Outlet boundary condition:

The outlet boundary is located at a distance of 100 h downstream of the step. The pressure is set to a constant value of $p = 0$. In addition, to prevent backflow at the outlet boundary, the outflow direction is set to be perpendicular to the outlet boundary and pointing outwards.
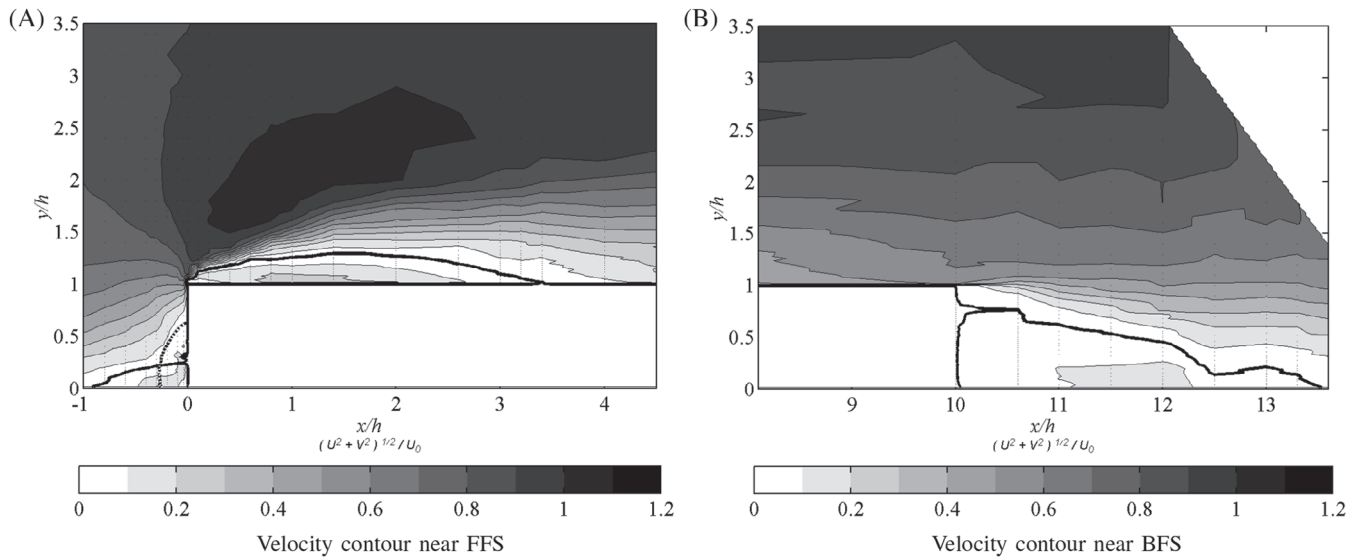
FIGURE 13 Experimental results from Leclercq et al.[37] Contours of the nondimensional modulus $(U^2 + V^2)^{1/2}/U_0$ of the statistically averaged mean velocity near the forward-facing step; the thick black lines denote mean locations of separation and reattachment

- Wall boundary condition:

  Slip boundary condition is applied to the upper boundary wall and nonslip boundary conditions to the rest of the channel walls.

- Initial boundary condition:

  As mentioned in the BFS flow case, the averaging solver is very sensitive to the initial condition. Here, the averaging solver also takes the solution of the instantaneous solver after a few iterations as the initial condition in order to prevent extreme values at the initial steps.

The unstructured mesh is created by the prepost processor GiD[33] and consisted of $19k$ elements. The detailed mesh configuration is to be found in Figures B1 and C1 in the Appendix.

5.2.3 | Results assessment

In addition to the BFS, an incompressible boundary layer flow over an FBFS produces extra complex dynamic behavior at the forward-facing step (FFS). Separations take place in two regions: one upstream and one downstream of the step face, both of which are subject to continuous buffeting from the surrounding flow and are highly unsteady. Due to the increase of the oncoming turbulence caused by the FFS, the recirculation zone behind the BFS in an FBFS flow is significantly shorter than that observed for single BFS flows which vary between six and eight step heights.[42]

In the following, the results of the averaging solver are compared with the results of the instantaneous solver and its directly averaged result and validated with the experimental results from Leclercq et al.[37]

The time-mean length of separation region is an important parameter characterizing the FBFS flow. In the flow investigated by Leclercq et al., the step trailing edge is located downstream of the reattachment of its leading edge. Figure 13 presents the experimental result of the modulus of the statistically averaged mean velocity scaled on the free stream velocity near the FFS and BFS. It can be seen from Figure 13(A) that the flow is first accelerated towards the FFS and then separated into two bubbles on either side of the FFS. The mean locations of separation and reattachment are denoted by thick black lines. A recirculation region can be seen upstream of the step leading edge. In Figure 13(B), it can be seen that the flow separates again at the edge of the BFS and reattaches at about 3.5 h downstream from the step.

Figure 14 presents a snap shot of velocity vectors near the step. A primary recirculation zone can be observed at the step leading edge, with the separation and reattachment positions in good agreement with the experimental result shown in Figure 13. The secondary recirculation zone fluctuates and vanishes. The sharp corner at the trailing edge initiates
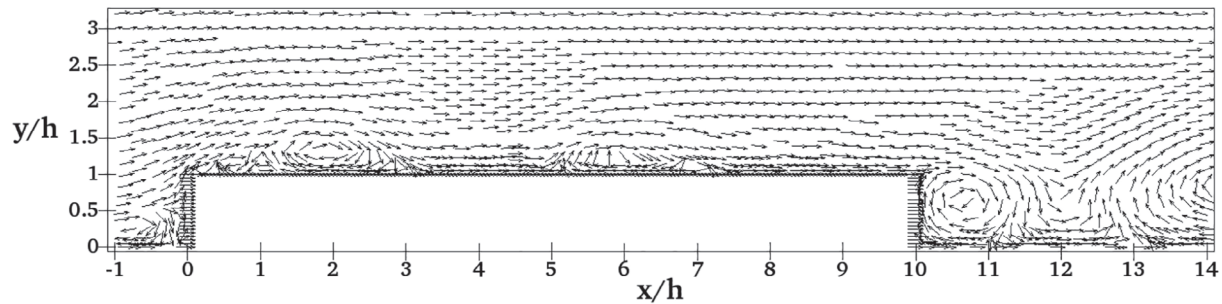
FIGURE 14 Vector plot of the instantaneous velocity near the step

another separation that extends 4–6 h downstream of the FFS step. This value is slightly overestimated compared with the experimental result found by Leclercq et al. which is approximately 3.5 h.

Figure 15 presents the time averaged flow field derived from the numerical solvers. The time averaging of the instantaneous solution indicates a time-mean length of 3.5 h of the recirculation zone at the FFS, which has a good agreement with the experimental result of a length of 3.2 h. At the BFS, a clear recirculation zone is observed with a length of 5.5 h, which is overestimated compared with the 3.5 h in the experiment. The solution of the time averaging solver is hardly distinguishable from the reference solution. The solution of the accelerated averaging solver correlates fairly well with the experimental result with a small overprediction on the recirculation length on the FFS and the BFS.

In other numerical investigations,[43–45] RANS models often failed to simulate this flow due to the unsteadiness of the flow structure. LES with a large number of time steps must be employed to obtain a statistically stationary state. Even more time steps are required to represent the time-mean length of the separation regions. In comparison, the presented solver shows much better robustness and efficiency with an accurate result in terms of the time-mean length of the recirculation zones.

5.3 | 2D flow over a cylinder with vortex shedding

Flow over a circular cylinder is a well-studied example in both experiments and numerical analysis. Despite the simplicity of the geometry, it is still one of the most challenging tasks as it combines adverse pressure, flow separation, transitions to turbulent boundary layer and vortex shedding. For a large range of Reynolds numbers, although the flow approaching the cylinder is steady and uniform, large eddies are shed alternately and continuously from the two sides of the cylinder forming a so-called von Karman vortex street. This makes the flow over a cylinder a very challenging and interesting case where the traditional RANS models fail and time averaged results can only be derived in a posteriori by averaging the instantaneous results from either URANS or LES simulations.[46–48]
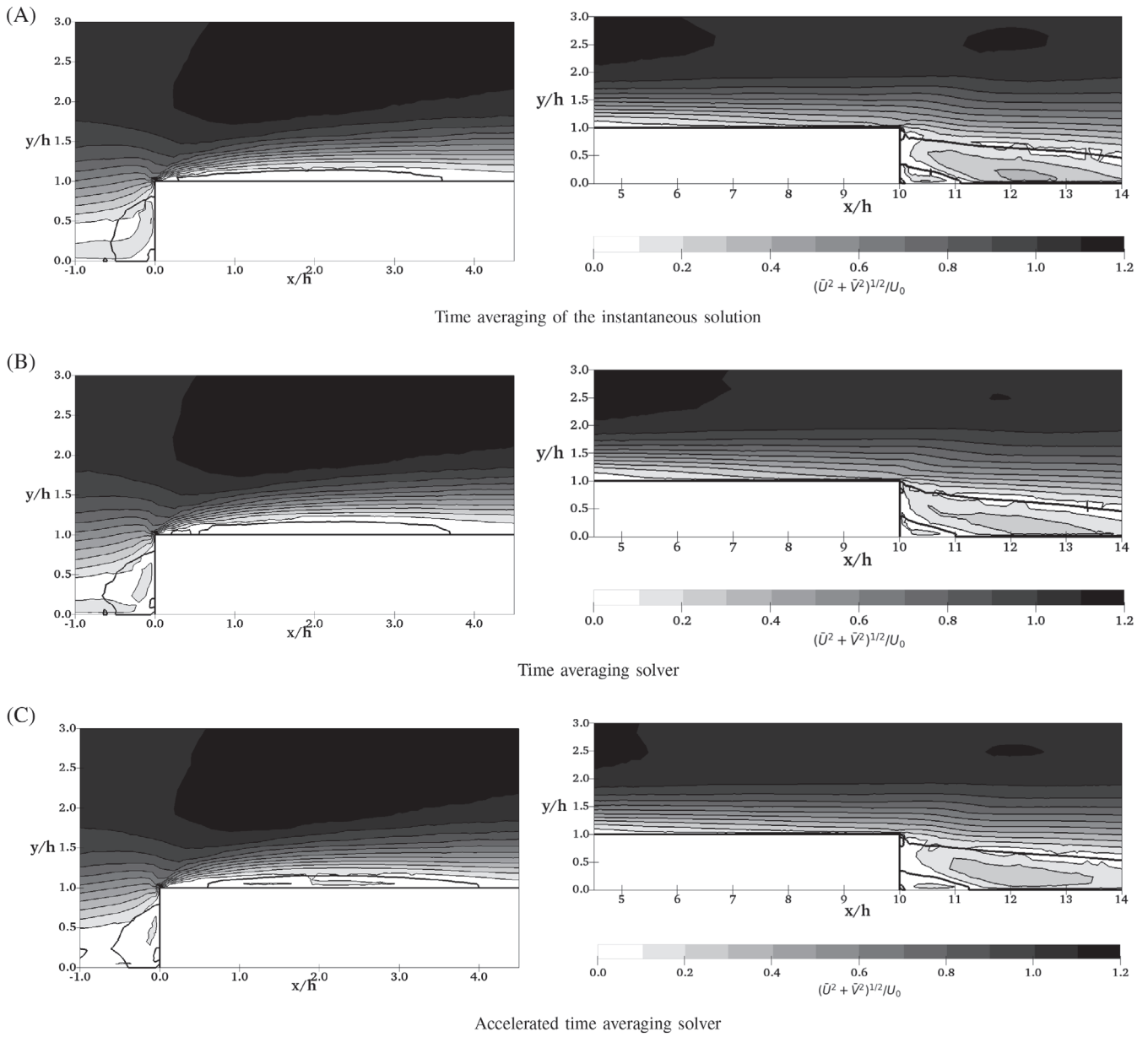
The flow pattern in the wake and its existence depends on the Reynolds number of the flow. With a low Reynolds number Re < 0.5, there is a minimal flow separation and the flow is considered to be steady. As the Reynolds number is increased to 2 < Re < 30, the boundary layer begins to separate symmetrically while the flow remains steady. The wake begins to oscillate periodically when the Reynolds number increases further to 40 < Re < 70. Above a Reynolds number of Re > 90, the eddies break off from the cylinder and start to continuously shedding alternately from the two sides of the cylinder and form the vortex street.[49] Beyond a Reynolds number of Re > 300, the vortex street become fully turbulent.[50]

In the numerical investigation, both laminar Re = 185 and turbulent vortex street Re = 3900 are analyzed with 2D simulations and their results compared with experimental results.

5.3.1 | Numerical setup

The numerical setup tries to reproduce a wind tunnel experiment of a steady uniform flow over a long circular cylinder. The computational domain is considerably large so that the farfield, as well as the pressure outlet boundary conditions, can be fulfilled and the vortex street can be captured. The schematic of the numerical setup is to be found in Figure 16.

(A)

Time averaging of the instantaneous solution

(B)

Time averaging solver

(C)

Accelerated time averaging solver

FIGURE 15 Contours of the nondimensional velocity modulus near the backward facing step marked with separation and reattachment regions

FIGURE 16 Numerical setup of a uniform steady flow over a two-dimensional cylinder
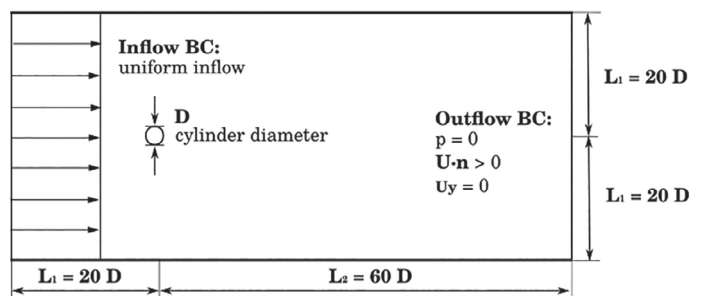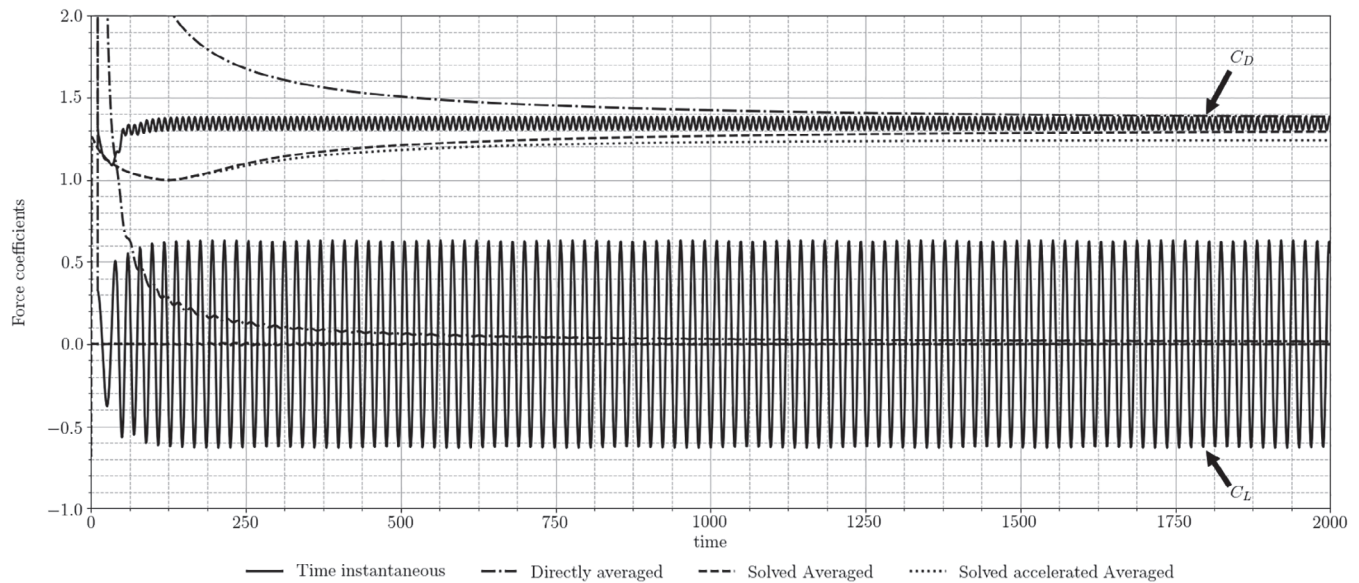
FIGURE 17 Lift and drag coefficients for a nonoscillating cylinder at Re = 185

- Inlet boundary condition:
  Constant velocity is applied on the inlet boundary, the magnitude of which is calculated based on the Reynolds number.

- Outlet boundary condition:
  The outlet boundary located at a distance of $60 \cdot D$ downstream from the cylinder to ensure that the wake is captured. The pressure set to a constant value of $p = 0$. In addition, to prevent back-flow at the outlet boundary, the outflow direction set to be perpendicular to the outlet boundary and pointing outwards.

- Wall boundary condition:
  Slip boundary condition applied on the upper boundary wall and nonslip boundary conditions on the cylinder.

- Initial boundary condition:
  As explained in the other cases, the averaging solver takes the solution from the instantaneous solver after some iterations as the initial condition to prevent extreme values in pressure at the initial steps to accelerate convergence.

The mesh applied in the numerical analysis is unstructured and is also created by GiD.[33] For the case of Re = 185, a grid consisting of 29k elements is employed, while for Re = 3900, a finer grid with 49k elements is employed. The detailed mesh configuration for this case is presented in Figure C3 in the Appendix.

5.3.2 | Results assessment: Re = 185

With this Reynolds number, the boundary layer is laminar over the front part of the cylinder and the separates over the back part of the cylinder. Eddies are shed off periodically in the wake of the cylinder.

Again, three solvers are employed, with the averaging solvers being to compared with the instantaneous solver and its directly averaged results as reference values. The computed time instantaneous flow is characterized by a stable, symmetric and periodic vortex shedding, which can be found in the Appendix. There are two fixed stagnation points at the front and back of the cylinder, which can also be observed in the time averaged solution.

The time histories of the lift and drag coefficients derived from different solvers are presented in Figure 17. It can be seen that both the lift and drag coefficients derived from the time instantaneous solution settle into a regular sinusoidal function after the onset of wake instability leading to the vortex shedding, whereas the time averaged coefficients derived directly from the instantaneous solver and coefficients derived from the averaging solvers gradually converge to the mean value of the instantaneous solver. The numerical results are also compared with experimental results and other numerical

T A B L E 5 Numerical and experimental values of C_D and $C_{L\,r.m.s}$ at Re $= 185$ after 2000 s

	$\overline{C_D}$	$C_{L\,r.m.s}$	Temporal iterations	Elapsed time
Experiment	1.28	–	–	–
Instantaneous solver	1.31	0.4236	16,647	2646 m
Averaging solver	1.29	0.0022	11,691	946 m
Accelerated averaging solver	1.24	0.0016	9232	787 m
Numerical result Lu and Dalton[51]	1.31	0.422		

results. The time averaged drag forces, the root mean square (r.m.s) value of the lift coefficients and the iteration steps required by the different solvers are shown in Table 5.

As the results in Table 5 show, the instantaneous solver slightly overpredicts the time averaged drag coefficient compared with the experimental result. However, this result confirms the previous findings in the literature from Lu and Dalton[51] in the averaged drag coefficient and the root mean square of the lift coefficient. The present averaging solver has a good agreement with the reference solver. Nevertheless, the averaging solver damps observably much faster to the mean value of the oscillating coefficients, as seen in Figure 17. This is also validated in Table 5 that both averaging solvers have a much smaller root mean square value of the lift coefficients than others. With the accelerated averaging solver, the total nonlinear iteration numbers required is reduced by half. Figure 18 presents the time averaged streamlines and pressure contour lines derived from the numerical solution. As expected, the averaging solver shares similar results with the reference solver in terms of the wave length and the positions of the wake centers. The pressure behind the cylinder predicted by the averaging solver is marginally higher than that of the reference solver, which can also be confirmed from Table 5 that the mean drag coefficient predicted by the averaging solver is smaller than that by the reference solver. Comparing the accelerated averaging solver with the averaging solver, the wake behind the cylinder is extended downstream-wise, which corresponds to denser pressure contour lines behind the cylinder. This results in a lower drag coefficient.

The plot of the nonlinear iteration numbers within a temporal step versus time shown in Figure 19 shares a clear similarity with the 1D nonlinear oscillator example shown in Figure 1 and the plot of BFS flow shown in Figure 7. The choice of the time step size of both instantaneous solver and the averaging solver is based on a constant overall maximum CFL number of 1. The onset of the vortex street can be seen at the point where the instantaneous solver reaches minimum time step size and where the slope of the time step size of the averaging solver reaches its maximum in magnitude. As a result of the alternating vortex shedding, the time step size variation of instantaneous solver shares a similar oscillation in the force coefficients in Figure 19, compared with which the time step size variation of the averaging solver is rather steady, indicating that the change of time averaged flow quantities is smaller. Two advantages of the averaging solver over the instantaneous solver can be observed. One advantage is the reduction of extreme values, In return, the overall time step size is increased and the solution is accelerated. Another advantage can be seen from the internal nonlinear iteration plot that the problem solved by the averaging solver is more linear than the original problem and the problem more linearized over time. This is also reflected in Table 5 that the CPU time for the averaging solver is by far shorter than that of the instantaneous solver. Despite a lower average number of nonlinear iterations per temporal step compared with the reference solver, the number of nonlinear iterations required by the accelerated averaging solver increases when the time step size increases too fast, which limits the choice of the growth ratio to a value of 1.05. To ensure a stable solution, the accelerated averaging solver only increases the time step size, when the number of nonlinear iterations falls below 7. Therefore, the speedup of the accelerated averaging solver over the reference solver is limited for flow with shedding vortexes.

5.3.3 | Results assessment: Re = 3900

With Re $= 3900$, the flow falls into the lower subcritical region, in which the flow remains laminar before the separation and the transition takes place in the wake with a fully turbulent vortex street. Figure 20 shows the force coefficients derived from different solvers. Compared with the laminar vortex street with Re $= 185$, the lift and drag amplitudes increase with the increasing Reynolds number. Figure 20 presents the drag and lift coefficients for this case. The time mean drag coefficient $\overline{C_D}$, the r.m.s value of the lift coefficient $C_{L\,r.m.s}$ are reported in Table 6. These values are compared with the

(A)

Time averaging of the instantaneous result

(B)

Averaging solver

(C)

Accelerated averaging solver
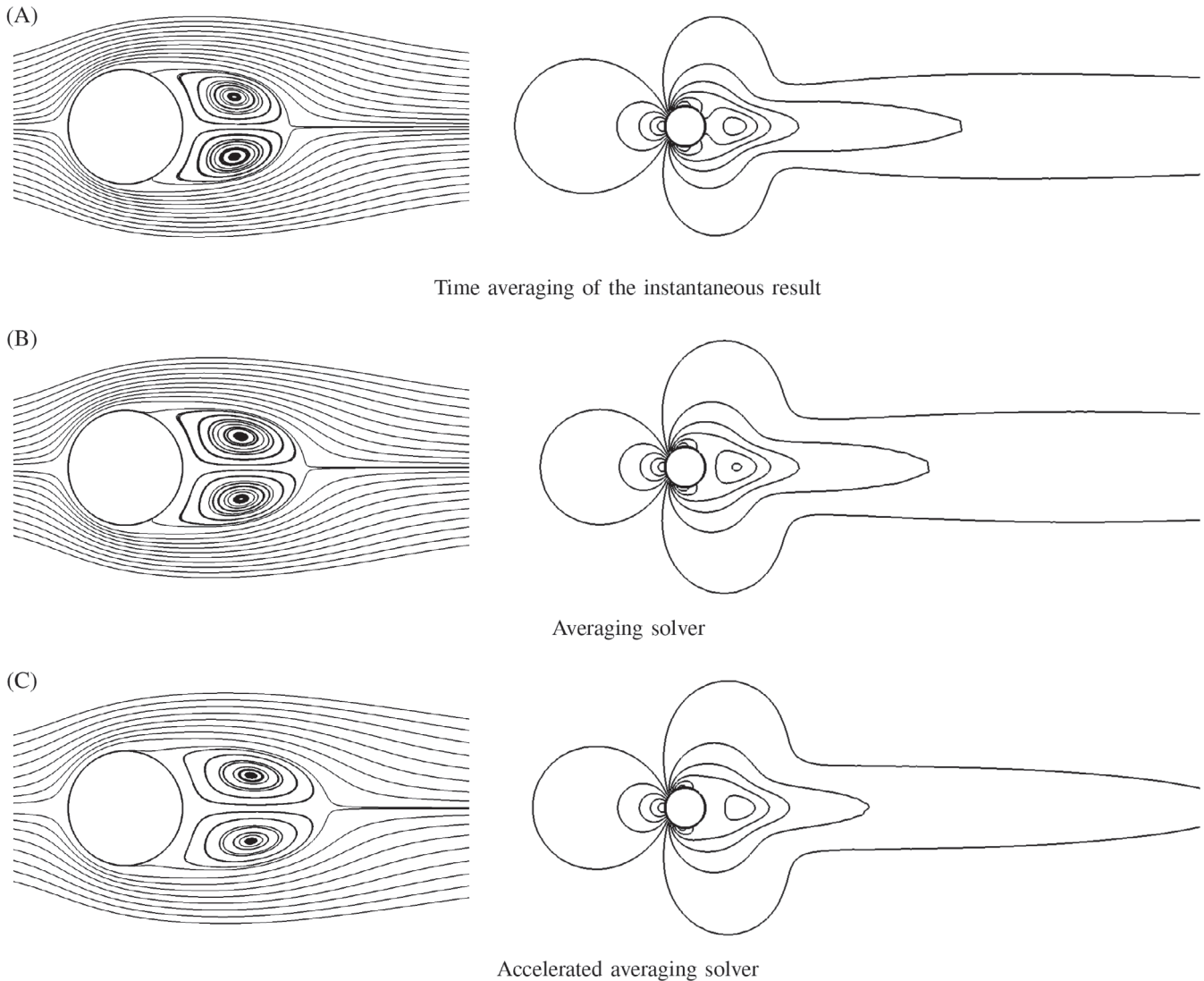
FIGURE 18 Streamlines and pressure coefficient isolines in interval of [−1.3:0.2:1.1] from different solvers of flow over cylinder at Re = 185

values reported in Shim et al.[52] for 2D and 3D cases. With Re = 3900, the drag and lift forces behave regularly as soon as the vortex shedding is established. The r.m.s value of the lift coefficient derived from the instantaneous solver is much larger than that from the experiment, which can also be observed in Figure 20, that the lift coefficient has a much larger amplitude.

The results differ from the experimental results. However, we should take into account that the simulations are solved in 2D. Williamson[53] and Karniadakis and Triantafyllou[54] have shown that at Re ≈ 200, the physics of the flow phenomenon is definitely not 2D. Besides, numerical studies show that the error of drag prediction increases with increasing Reynolds numbers.[47] Therefore, modeling the flow with 2D simulations at a relatively high Reynolds number of Re = 3900 delivers poor results. Nevertheless, the goal of testing the flow over a cylinder at a higher Reynolds number is to estimate the robustness and the accuracy of the averaging solver in the sense that a steady state solution can be delivered despite high unsteadiness and that the averaging solver's solution matches the direct average of the instantaneous solver. Comparing the 2D URANS and 3D URANS results from Shim et al.,[52] it can be confirmed that a 3D simulation delivers a much more realistic result. Nevertheless, Shim et al. state that 3D URANS still cannot capture all flow features. Therefore, 3D LES simulations are required to have a good agreement with experimental results. Comparing the current approach with URANS for the cylinder flow problems, it is not possible for URANS to faithfully reproduce the instabilities of the shear layers due to the deficient transition-modeling of most RANS models.[47,48,52] This statement is supported
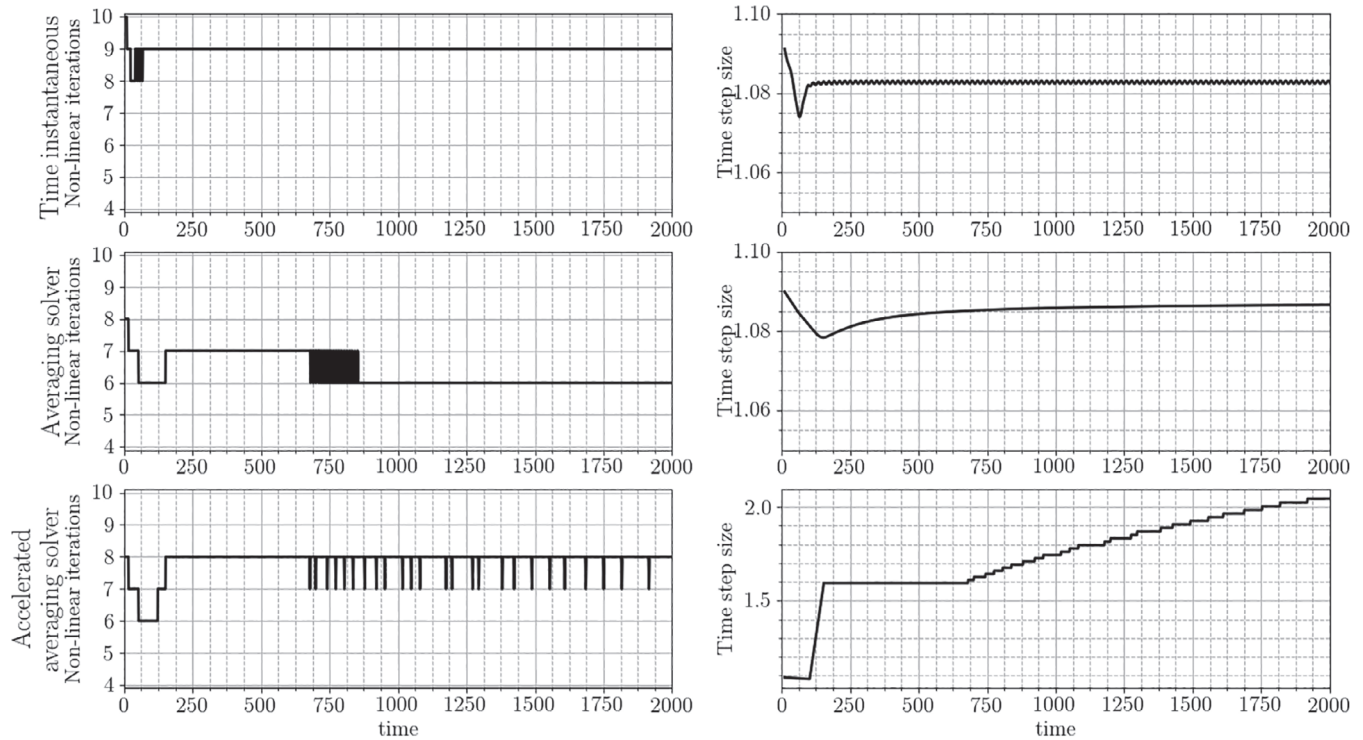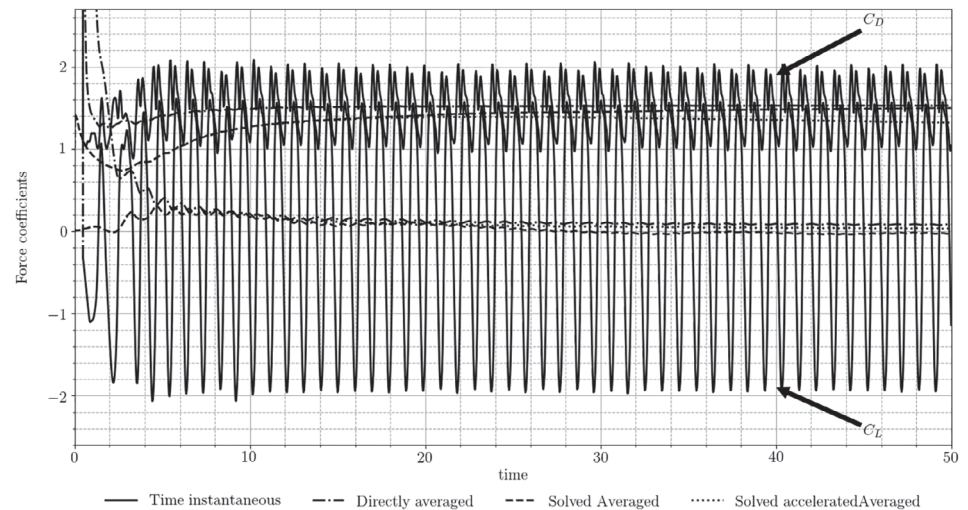
FIGURE 19 Plot of nonlinear iteration numbers over time of a flow over cylinder at Re = 185 at $t = 2000$ s

FIGURE 20 Lift and drag coefficients for a flow over cylinder at Re = 3900

by the results shown in Table 6 that the current 2D result agrees better with the experimental result than the 2D RANS result from Shim et al.[52]

In fact, for Re > 1000, secondary vortices are developed together with a trail of small eddies that merge with the larger ones in the shear layers,[48] which can be observed in a time averaged sense in Figure 21. Compared with the time averaged streamlines from Re = 185 in Figure 18, the wake of Re = 3900 in Figure 21 has two recirculation centers instead a single one and is much shorter in length.

The streamlines derived by the three solvers are different from each other. Nevertheless, they provide comparable pressure contours. Due to the high turbulence and unsteadiness, the time averaging of the instantaneous has difficulties delivering symmetrical streamlines, while both averaging solvers show symmetrical streamlines with two recirculation centers which are also reported in Shim et al.[52] Comparing the accelerated averaging solver with the averaging solver, the wave length is overestimated. The pressure in front of the cylinder predicted by the accelerated solver is smaller compared with that by the reference solver and the averaging solver, leading to a lower $\overline{C}_\mathrm{D}$ value in Table 6.

**TABLE 6** Numerical and experimental values of C_D and $C_{L\,r.m.s}$ at Re = 3900

	$\overline{C}_D$	$C_{L\,r.m.s}$	Temporal iterations	Elapsed time
Experiment	0.98	0.03–0.08	–	–
Instantaneous solver	1.53	1.274	13,629	1208 m
Averaging solver	1.50	0.103	5524	609 m
Accelerated averaging solver	1.36	0.126	3706	421 m
2D URANS result Shim et al.[52]	1.59	1.17		
3D URANS result Shim et al.[52]	1.32	0.701		
3D LES result Shim et al.[52]	1.03	0.908		

Abbreviations: LES, large Eddy simulation; URANS, unsteady Reynolds-averaged Navier–Stokes.

(A)

Time averaging of the instantaneous result

(B)

Averaging solver

(C)

Accelerated averaging solver
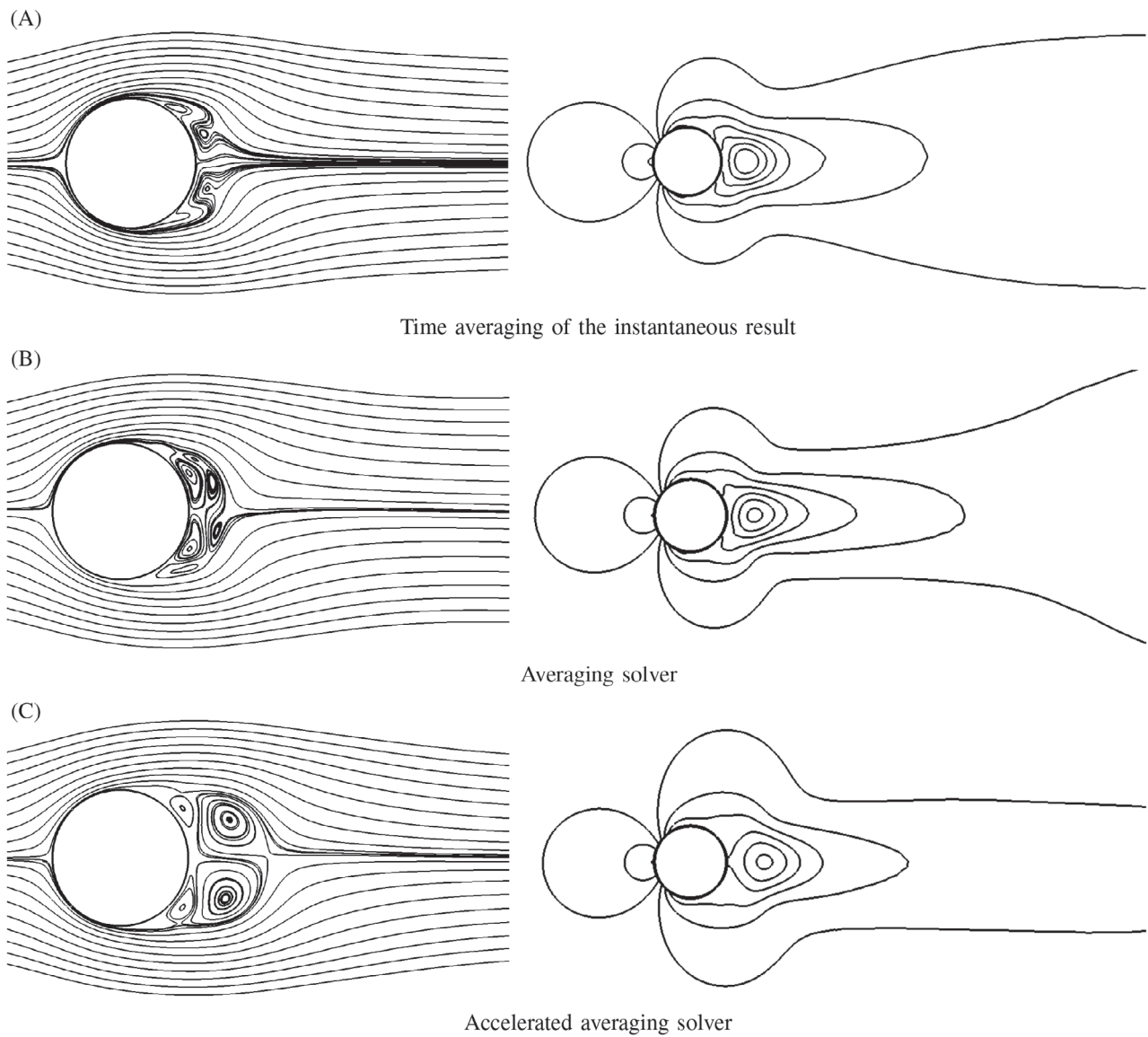
FIGURE 21 Streamlines and pressure coefficient isolines in interval of [−3:0.4:1] from different solvers of flow over cylinder at Re = 3900 at t = 50 s
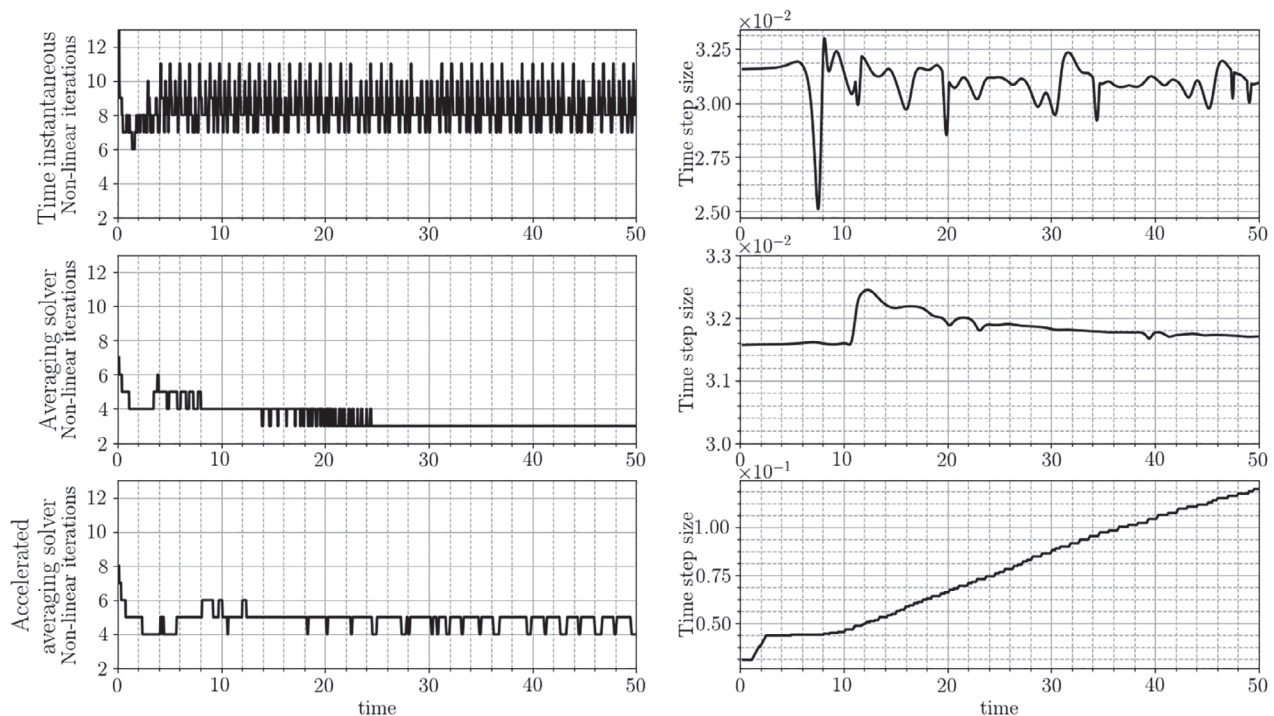
FIGURE 22 Plot of nonlinear iteration numbers over time of a flow over cylinder at Re = 3900

Taking a look at the nonlinear iterations needed within each temporal step over time in Figure 22, the flow problem is considerably more nonlinear as more iterations are required in each temporal step than in the case of the laminar vortex street. One interesting point is that compared with the laminar case, the number of nonlinear iterations per step is reduced by a much larger amount, which indicates that the averaging technique improves the problem condition better with higher Reynolds number. It should be noted, however, that as the Reynolds number increases, the accelerated averaging solver is more sensitive to the time step growth ratio, which limits the improvement of the accelerated averaging solver.

6 | CONCLUSION

A time averaging technique is introduced aiming at deriving a fast time averaged solution. This approach directly solves the time averaged flow quantities instead of the time instantaneous flow quantities. The new capabilities improve the robustness and efficiency of simulating an unsteady flow field and significantly reduce the computational time. Another positive feature is that the investigated strategy does not require any specific LES closure. In the present article, the VMS approach has been applied in the hybridization strategy for the closure of the LES part, with an ASGS model. The concept of the averaging technique and its acceleration methods are demonstrated with a hands-on nonlinear 1D oscillator analytical example.

Many numerical investigations are conducted comparing the averaging technique against the conventional methods for different types of flows, ranging from laminar flow to strongly turbulent flows, covering most of the unsteady effects in flow analysis. A clear advantage of the averaging technique in achieving time averaged results is observed. In the case of BFS, a detailed analysis is carried to prove the accuracy and convergence to the steady state. The averaging solver has shown a faster convergence to the time averaged steady state solution with a lower computational cost. The predictions of the main flow parameters agree well with the experimental results and other simulation results in the literature. In the case of FBFS, it is shown that the averaging solver is capable of solving flow problem with inherent unsteadiness where RANS usually suffers from convergence problems. In the case of the flow over a cylinder with vortex shedding where the URANS models are not able to reproduce the detailed flow structures, the averaging solver with VMS provides a good comprehensible solution between efficiency and accuracy. Notwithstanding the lack of agreement in the high Reynolds number cases, these results are encouraging in the perspective of the application of the same methodology to the simulation of complex engineering problems, such as flows over tube arrays or components of offshore platforms, to get a fast time averaged solution.

An important remark is that turbulence is inherently a 3D problem, while the investigation in current article only covers 2D test cases, which are chosen to minimize the computational effort. We observe, however, that large eddies have a lower dissipation rate in the 2D case than in the 3D case, a feature that is not beneficial for the approach under investigation. Our point here is that, pending a future verification, we see no reason for which the technique cannot be extended to the 3D case. Our hope is actually that the method may even be more effective in cases in which large eddies dissipate faster than in the ones that are chosen here.

Another remark for the time averaging technique is that it can be generalized other spatial discretization schemes, such as FDM and FVM, though it has only been applied to FEM in this article. In the end, this article provides a new time averaging time integration scheme, which is independent of the underlying spatial discretization.

In conclusion, the averaging technique shows a clear advantage over the reference solver in terms of improvements in computational efficiency with good accuracy in determining time averaged solutions. The accelerated averaging solver helps to further reduce the simulation time, however, at the expense of accuracy. More research is needed to determine a better strategy to speed up the averaging solver while minimizing the loss of accuracy. Further investigations are also needed to better understand the stability problem occurred when accelerating the averaging solver at high Reynolds number.

DATA AVAILABILITY STATEMENT
The datasets generated during and analyzed during the current study are available from the corresponding author on reasonable request. The code used to generate the datasets is available in the Kratos Multiphysics repository (https://github.com/KratosMultiphysics/Kratos).

ORCID
Mengjie Zhao https://orcid.org/0000-0002-2210-4455
Rubén Zorrilla https://orcid.org/0000-0001-8270-7170

REFERENCES
1. Witherden FD, Jameson A. Future directions in computational fluid dynamics. Paper presented at: Proceedings of the 23rd AIAA Computational Fluid Dynamics Conference, Denver, Colorado; February 2017. https://doi.org/10.2514/6.2017-3791.
2. Ward-Smith J. *Mechanics Fluids E8: Solutions*. Oxfordshire: Taylor & Francis Ltd; 2005.
3. Dadvand P, Rossi R, Oñate E. An object-oriented environment for developing finite element codes for multi-disciplinary applications. *Arch Comput Methods Eng*. 2010;17(3):253-297.
4. Dadvand P, Rossi R, Gil M, et al. Migration of a generic multi-physics framework to HPC environments. *Comput Fluids*. 2013;80:301-309.
5. Zienkiewicz OC, Taylor RL, Nithiarasu P. *The Finite Element Method for Fluid Dynamics*. Oxford; Butterworth-Heinemann; 2014.
6. John V. The space averaged Navier-Stokes equations and the commutation error. Lecture Notes in Computational Science and Engineering Large Eddy Simulation of Turbulent Incompressible Flows; 2004:21-46.
7. Sagaut P. *Large Eddy Simulation for Incompressible Flows*. New York, NY: Springer; 2002.
8. Hughes TJ. Multiscale phenomena: greens functions, the Dirichlet-to-Neumann formulation, subgrid scale models, bubbles and the origins of stabilized methods. *Comput Methods Appl Mech Eng*. 1995;127(1-4):387-401.
9. Codina R. Stabilized finite element approximation of transient incompressible flows using orthogonal subscales. *Comput Methods Appl Mech Eng*. 2002;191(39-40):4295-4321.
10. Codina R. A stabilized finite element method for generalized stationary incompressible flows. *Comput Methods Appl Mech Eng*. 2001;190(20-21):2681-2706.
11. J. Cotela Dalmau, *Applications of Turbulence Modeling in Civil Engineering* [PhD thesis]. UPC, Departament de Resisténcia de Materials i Estructures a l'Enginyeria; 2016.
12. Curtiss CF, Hirschfelder JO. Integration of stiff equations. *Proc Nat Acad Sci US Am*. 1952;38(3):235.
13. Layton W, Mays N, Neda M, Trenchea C. Numerical analysis of modular regularization methods for the BDF2 time discretization of the Navier-Stokes equations. *ESAIM Math Modell Numer Anal*. 2014;48(3):765-793.
14. Forti D, Dedé L. Semi-implicit BDF time discretization of the Navier-Stokes equations with VMS-LES modeling in a high performance computing framework. *Comput Fluids*. 2015;117:168-182.

15. Celaya EA, Aguirrezabala JJA, Chatzipantelidis P. Implementation of an adaptive BDF2 formula and comparison with the matlab ode15s. Paper presented at: Procedings of Computer Science International Conference on Computational Science, Cairns, Australia; vol. 29, 2014:1014-1026. https://doi.org/10.1016/j.procs.2014.05.091.

16. Wang D, Ruuth SJ. Variable step-size implicit-explicit linear multistep methods for time-dependent partial differential equations. *J Comput Math*. 2008;26:838-855.

17. Jannelli A, Fazio R. Adaptive stiff solvers at low accuracy and complexity. *J Comput Appl Math*. 2006;191(2):246-258.

18. Denner AK. *Experiments on temporal variable step BDF2 algorithms* [Master's thesis]; 2014.

19. Ben-Israel A. A newton-raphson method for the solution of systems of equations. *J Math Anal Appl*. 1966;15(2):243-252.

20. Kim J, Moin P. Application of a fractional-step method to incompressible Navier-Stokes equations. *Journal of Computational Physics*. 1985;59(2):308-323. http://dx.doi.org/10.1016/0021-9991(85)90148-2.

21. Sohn J. L.. Evaluation of FIDAP on some classical laminar and turbulent benchmarks. *International Journal for Numerical Methods in Fluids*. 1988;8(12):1469-1490. http://dx.doi.org/10.1002/fld.1650081202.

22. Gartling DK. A test problem for outflow boundary conditions–flow over a backward-facing step. *Int J Numer Methods Fluids*. 1990;11(7):953-967.

23. Gresho Philip M., Gartling David K., Torczynski J. R., Cliffe K. A., Winters K. H., Garratt T. J., Spence A., Goodrich John W.. Is the steady viscous incompressible two-dimensional flow over a backward-facing step at Re = 800 stable?. *International Journal for Numerical Methods in Fluids*. 1993;17(6):501-541. http://dx.doi.org/10.1002/fld.1650170605.

24. Armaly BF, Durst F, Pereira JCF, Schönung B. Experimental and theoretical investigation of backward-facing step flow. *J Fluid Mech*. 1983;127(1):473.

25. Durst F, Tropea C. Flows over two-dimensional backward facing steps. *Struct Complex Turbulent Shear Flow*. 1983;142:41-52.

26. Moss WD, Baker S, Bradbury LJS. Measurements of mean velocity and Reynolds stresses in some regions of recirculating flow. *Turbulent Shear Flows I*. Berlin, Heidelberg: Springer; 1979;198-207. https://doi.org/10.1007/978-3-642-46395-2_15.

27. Fortin A, Jardak M, Gervais JJ, Pierre R. Localization of hopf bifurcations in fluid flow problems. *Int J Numer Methods Fluids*. 1999;24(11):1185-1210. https://doi.org/10.1002/(SICI)1097-0363(19970615)24:111185::AID-FLD5353.0.CO;2-X.

28. Barkley D, Gomes MGM, Henderson RD. Three-dimensional instability in flow over a backward-facing step. *J Fluid Mech*. 2002;473:167-190.

29. Abe K, Kondoh T, Nagano Y. A new turbulence model for predicting fluid flow and heat transfer in separating and reattaching flows–I. flow field calculations. *Int J Heat Mass Transf*. 1994;37(1):139-151.

30. Craft T. Developments in a low-Reynolds-number second-moment closure and its application to separating and reattaching flows. *Int J Heat Fluid Flow*. 1998;19(5):541-548.

31. Parneix S, Laurence D, Durbin PA. A procedure for using DNS databases. *J Fluids Eng*. 1998;120(1):40.

32. Erturk E. Numerical solutions of 2-d steady incompressible flow over a backward-facing step, part I: high Reynolds number solutions. *Comput Fluids*. 2008;37(6):633-655.

33. Gid -The personal pre and post processor. 2008.

34. Biswas G, Breuer M, Durst F. Backward-facing step flows for various expansion ratios at low and moderate Reynolds numbers. *J Fluids Eng*. 2004;126(3):362.

35. Malamataris NA. A numerical investigation of wall effects in three-dimensional, laminar flow over a backward facing step with a constant aspect and expansion ratio. *Int J Numer Methods Fluids*. 2012;71(9):1073-1102.

36. Becker J. A second order backward difference method with variable steps for a parabolic problem. *BIT Numer Math*. 1998;38(4):644-662.

37. Leclercq D, Jacob M, Louisot A, Talotte C. Forward-backward facing step pair - aerodynamic flow, wall pressure and acoustic characterisation. Paper presented at: Proceedings of the 7th AIAA/CEAS Aeroacoustics Conference and Exhibit, Maastricht, Netherlands; 2001. https://doi.org/10.2514/6.2001-2249.

38. Moss W, Baker S. Re-circulating flows associated with two-dimensional steps. *Aeronautical Quart*. 1980;31(03):151-172.

39. Schlichting H. Gersten Klaus, *Boundary-Layer Theory*. 7th ed. Berlin, Heidelberg: Springer; 2017. https://doi.org/10.1007/978-3-662-52919-5.

40. Duncan WJ, Thom AS, Young AC. *Mechanics of Fluids*. London: Arnold; 1985.

41. Afzal N. Power law and log law velocity profiles in turbulent boundary-layer flow: equivalent relations at large Reynolds numbers. *Acta Mech*. 2001;151(3-4):195-216.

42. Farabee TM, Casarella MJ. Effects of surface irregularity on turbulent boundary layer wall pressure fluctuations. *J Vib Acoust Stress Reliab Design*. 1984;106(3):343.

43. Najjar FM, Vanka SP. Numerical study of a separated-reattaching flow. *Theoret Comput Fluid Dyn*. 1993;5(6):291-308.

44. Abdalla IE, Cook MJ. Spectral analysis of a transitional separated-reattached flow using fourier and wavelet transforms. *Computational Methods and Experimental Measurements*. Vol XIII; Ashurst Lodge: WIT Press; 2007;13.

45. Moreau DJ, Coombs JL, Doolan CJ. On the flow and noise of a two-dimensional step element in a turbulent boundary layer. *Fluid-Structure-Sound Interactions and Control Lecture Notes in Mechanical Engineering*; Berlin, Heidelberg: Springer; 2014:225-230. https://doi.org/10.1007/978-3-642-40371-2_33.

46. Zhang L, Wray T, Agarwal RK. Numerical simulation of flow past a circular and a square cylinder at high Reynolds number. Paper presented at: Proceedings of the 47th AIAA Fluid Dynamics Conference, Denver, Colorado; February 2017. https://doi.org/10.2514/6.2017-3322.

47. Rosetti GF, Vaz G, Fujarra ALC. URANS calculations for smooth circular cylinder flow in a wide range of Reynolds numbers: solution verification and validation. *Ocean Eng.* 2012;54:150-169.

48. Moussaed C, Salvetti MV, Wornom S, Koobus B, Dervieux A. Simulation of the flow past a circular cylinder in the supercritical regime by blending RANS and variational-multiscale LES models. *J Fluids Struct.* 2014;47:114-123.

49. Massey BS, Ward-Smith AJ. *Mechanics of Fluids.* Boca Raton, FL: CRC Press; 2018.

50. Blevins RD. *Flow-Induced Vibration.* Florida: Krieger Publishing Company; 2001.

51. Lu X-Y, Dalton C. Calculation of the timing of vortex formation from an oscillating cylinder. *J Fluids Struct.* 1996;10(5):527-541.

52. Shim YM, Sharma R, Richards P. Numerical study of the flow over a circular cylinder in the near wake at Reynolds number 3900. Paper presented at: Proceedings of the 39th AIAA Fluid Dynamics Conference, San Antonio, Texas; 2009. https://doi.org/10.2514/6.2009-4160.

53. Williamson C. Vortex dynamics in the cylinder wake. *Ann Rev Fluid Mech.* 1996;28:477-539.

54. Karniadakis GE, Triantafyllou GS. Three-dimensional dynamics and transition to turbulence in the wake of bluff objects. *J Fluid Mech.* 1992;238:1-30.

APPENDIX A. ELEMENT MATRICES OF THE STANDARD GALERKIN TERMS AND THE STABILIZATION TERMS FOR QUASI-STATIC ASGS FORMULATION

$$\mathbf{M_{ab}^e} = \int_{\Omega_e} \rho \mathbf{N}_a^T \mathbf{N}_b \ d\Omega, \tag{A1}$$

$$\mathbf{C(u)_{ab}^e} = \int_{\Omega_e} \rho \frac{1}{2} (\mathbf{N}_a^T \mathbf{u} \cdot \nabla \mathbf{N}_b - (\mathbf{u} \cdot \nabla \mathbf{N}_a)^T \mathbf{N}_b) \ d\Omega + \int_{\Omega_e} \mathbf{N}_a^T \rho \frac{1}{2} (\mathbf{u} \cdot \mathbf{n}) \mathbf{N}_b \ d\Gamma, \tag{A2}$$

$$\mathbf{K}_{ab}^e = \int_{\Omega_e} \rho \mathbf{B}_a^T \mathbf{C_\mu} \mathbf{B}_b \ d\Omega, \tag{A3}$$

$$\mathbf{G(u)}_{ab}^e = -\int_{\Omega_e} (\nabla \cdot \mathbf{N}_a)^T N_b \ d\Omega, \tag{A4}$$

$$\mathbf{D(u)}_{ab}^e = \int_{\Omega_e} N_a \nabla \cdot \mathbf{N}_b \ d\Omega = -(\mathbf{G}_{ba}^e)^T, \tag{A5}$$

$$\mathbf{F}_a^e = \int_{\Omega_e} \mathbf{N}_a^T \mathbf{f} \ d\Omega, \tag{A6}$$

$$\mathbf{T}_a^e = \int_{\Gamma_N} \mathbf{N}_a^T \mathbf{t} \ d\Gamma, \tag{A7}$$

$$\mathbf{S}_m(\tau_u, \mathbf{u})_{ab}^e = \int_{\Omega_e} (\rho \mathbf{u} \cdot \nabla \mathbf{N}_a)^T \tau_u \mathbf{N}_b \ d\Omega, \tag{A8}$$

$$\mathbf{S}_u(\tau_u, \mathbf{u})_{ab}^e = \int_{\Omega_e} (\rho \mathbf{u} \cdot \nabla \mathbf{N}_a)^T \tau_u \rho \mathbf{u} \nabla \cdot \mathbf{N}_b \ d\Omega, \tag{A9}$$

$$\mathbf{S}_p(\tau_u, \mathbf{u})_{ab}^e = \int_{\Omega_e} (\rho \mathbf{u} \cdot \nabla \mathbf{N}_a)^T \tau_u \nabla N_b \ d\Omega, \tag{A10}$$

$$\mathbf{S}_f(\tau_u, \mathbf{u})_{ab}^e = \int_{\Omega_e} (\rho \mathbf{u} \cdot \nabla \mathbf{N}_a)^T \tau_u \mathbf{f} \ d\Omega, \tag{A11}$$

$$\mathbf{Q}_m(\tau_u)_{ab}^e = \int_{\Omega_e} (\nabla \mathbf{N}_a)^T \tau_u \mathbf{N}_b \ d\Omega, \tag{A12}$$

$$\mathbf{Q}_u(\tau_u, \mathbf{u})_{ab}^e = \int_{\Omega_e} (\nabla \mathbf{N}_a)^T \tau_u \rho \mathbf{u} \cdot \nabla \mathbf{N}_b \ d\Omega, \tag{A13}$$

$$\mathbf{Q}_p(\tau_u)_{ab}^e = \int_{\Omega_e} (\nabla \mathbf{N}_a)^T \tau_u \nabla \mathbf{N}_b \ d\Omega, \tag{A14}$$

$$\mathbf{Q}_f(\tau_u)_{ab}^e = \int_{\Omega_e} (\nabla \mathbf{N}_a)^T \tau_u \mathbf{f} \ d\Omega, \tag{A15}$$

$$\mathbf{H}_u(\tau_p)_{ab}^e = \int_{\Omega_e} (\nabla \cdot \mathbf{N}_a)^T \tau_p \nabla \cdot \mathbf{N}_b \ d\Omega. \tag{A16}$$

APPENDIX B. MESH CONFIGURATIONS

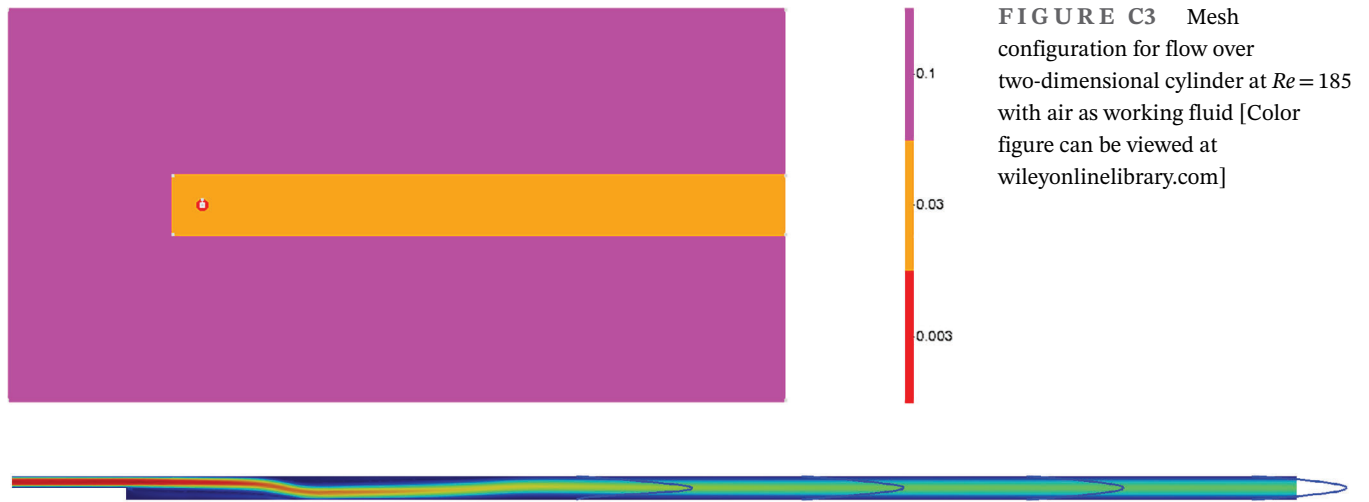**FIGURE B1**   Mesh configuration for backward facing step flow [Color figure can be viewed at wileyonlinelibrary.com]

APPENDIX C. 2D BACKWARD FACING STEP FLOW RESULTS

FIGURE C1   Mesh configuration for forward–backward facing step flow at high Reynolds number $Re = 6600$ [Color figure can be viewed at wileyonlinelibrary.com]
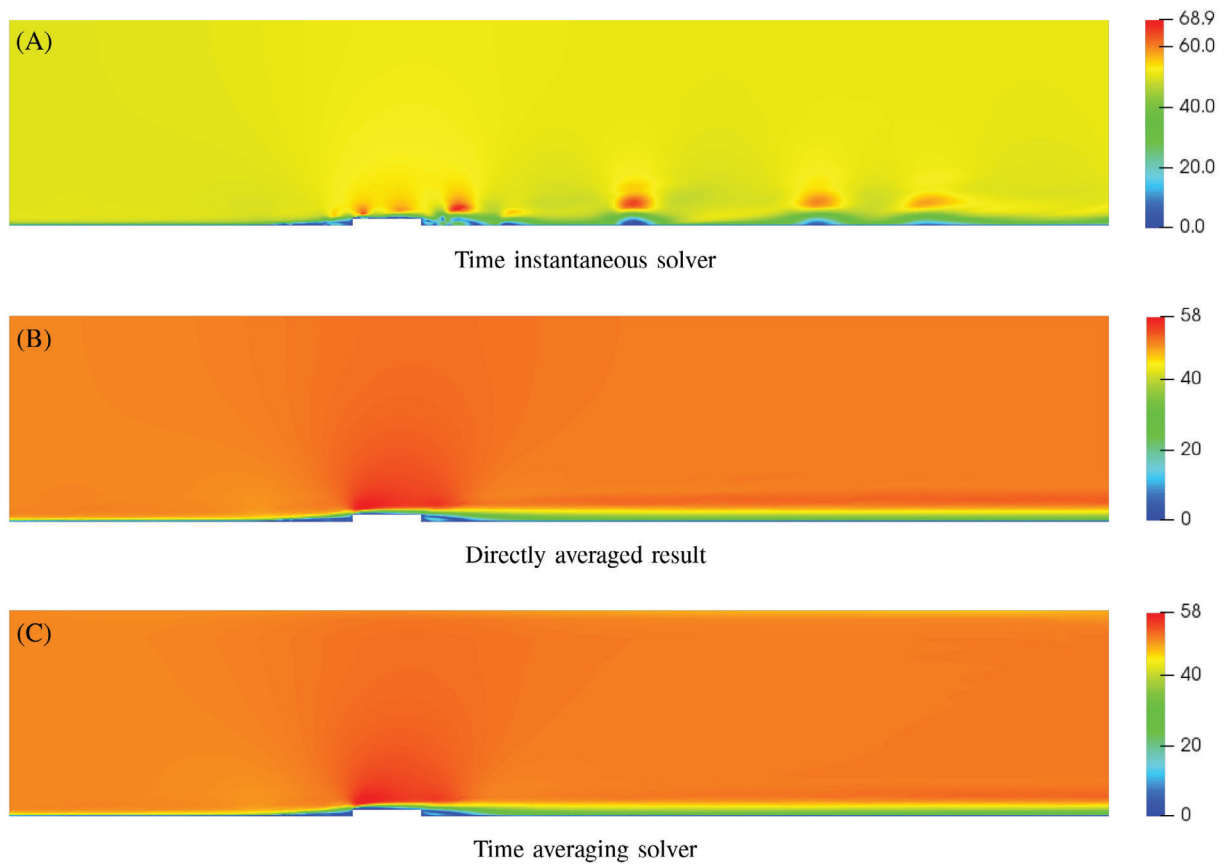

FIGURE C2   Mesh configuration for forward–backward facing step flow [Color figure can be viewed at wileyonlinelibrary.com]
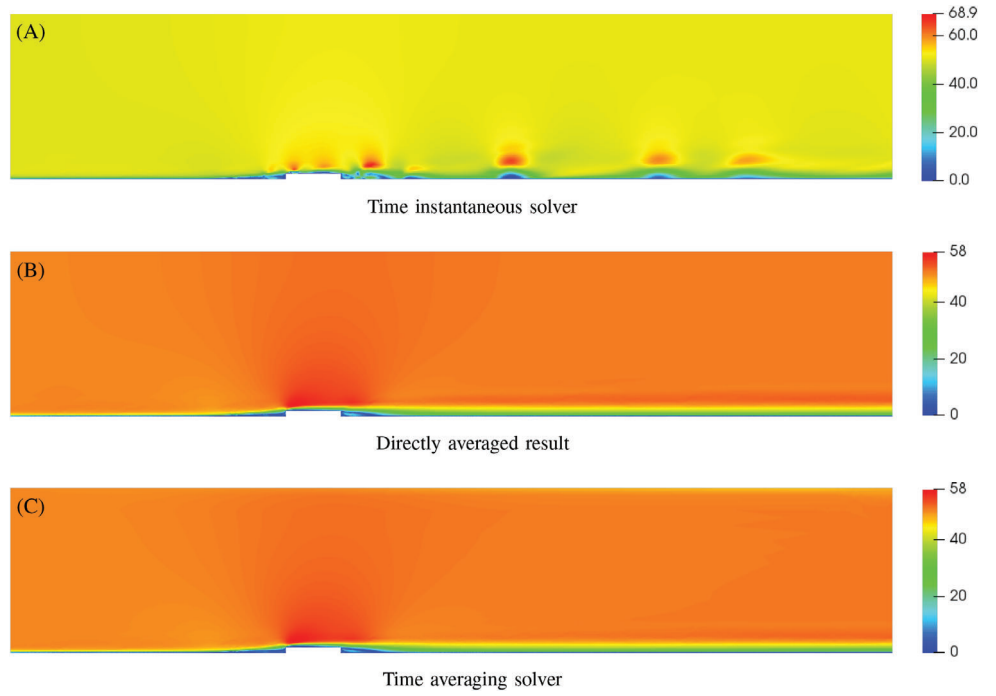
FIGURE C4 Fully developed flow at exit boundary [Color figure can be viewed at wileyonlinelibrary.com]

APPENDIX D. 2D FORWARD–BACKWARD FACING STEP FLOW RESULTS
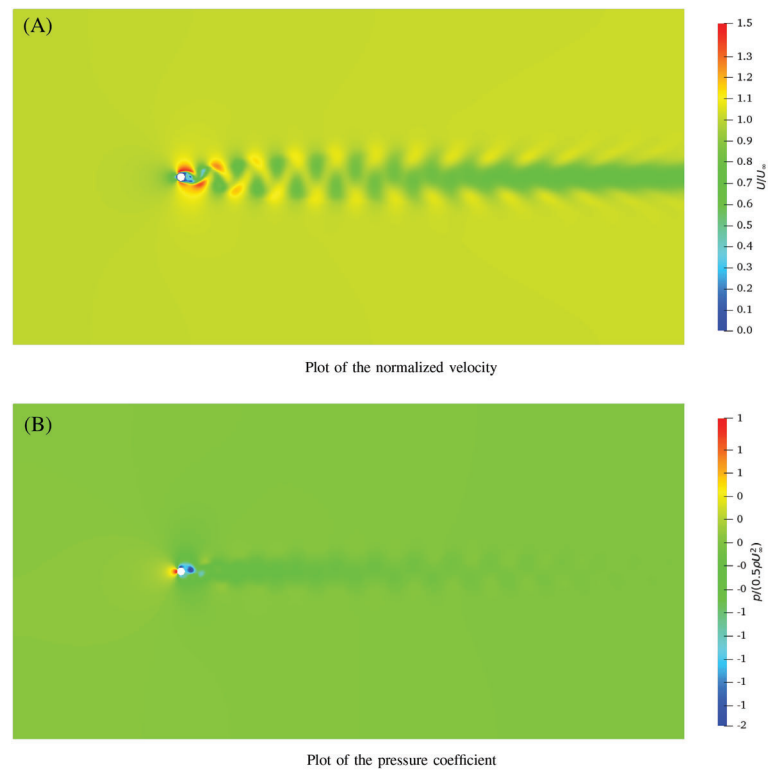

Time instantaneous solver

Directly averaged result

Time averaging solver

FIGURE D1 Velocity contour plot [Color figure can be viewed at wileyonlinelibrary.com]

FIGURE D2 Pressure contour plot [Color figure can be viewed at wileyonlinelibrary.com]

Time instantaneous solver

Directly averaged result

Time averaging solver

APPENDIX E. 2D FLOW OVER CYLINDER WITH VORTEX SHEDDING RESULTS

Plot of the normalized velocity

Plot of the pressure coefficient

FIGURE E1 Instant snapshot of the normalized velocity for a two-dimensional flow over cylinder at $Re = 185$ at $t = 2000$ s [Color figure can be viewed at wileyonlinelibrary.com]

(A)

Plot of the normalized velocity

(B)

Plot of the pressure coefficient

FIGURE E2 Instant snapshot of the normalized velocity for a two-dimensional flow over cylinder at $Re = 3900$ at $t = 50$ s [Color figure can be viewed at wileyonlinelibrary.com]